

# A Low-Rank QTT-based Finite Element Method for Elasticity Problems

Elena Benvenuti<sup>a</sup>, Gianmarco Manzini<sup>b,\*</sup>, Marco Nale<sup>a</sup>, Simone Pizzolato<sup>a</sup>

<sup>a</sup>*Department of Engineering, University of Ferrara, via Saragat 1, Ferrara, 44122, Italy*

<sup>b</sup>*Theoretical Division, Los Alamos National Laboratory, Los Alamos, NM 87545, United States of America*

---

## Abstract

We present an efficient and robust numerical algorithm for solving the two-dimensional linear elasticity problem that combines the Quantized Tensor Train format and a domain partitioning strategy. This approach makes it possible to solve the linear elasticity problem on a computational domain that is more general than a square. Our method substantially decreases memory usage and achieves a notable reduction in rank compared to established Finite Element implementations like the FEniCS platform. This performance gain, however, requires a fundamental rethinking of how core finite element operations are implemented, which includes changes to mesh discretization, node and degree of freedom ordering, stiffness matrix and internal nodal force assembly, and the execution of algebraic matrix-vector operations. In this work, we discuss all these aspects in detail and assess the method's performance in the numerical approximation of three representative test cases.

*Keywords:* Finite element method, tensor train format, quantized tensor train format, elasticity

---

## 1. Introduction

The numerical approximation of partial differential equations (PDEs) is pivotal in various scientific and engineering disciplines, for example, in structural mechanics, especially when dealing with complex geometries and singular solutions. Traditional numerical methods, such as the Finite Element Method (FEM), are widely recognized for their robustness and accuracy in handling such problems. However, the computational cost of these methods escalates rapidly with increasing problem size and complexity, often rendering high-resolution simulations impractical on conventional hardware.

Several strategies have been developed to address computational resource limitations and efficiency. Order reduction methods such as Ladèveze's LATIN method [1, 2] and the Proper Generalized Decomposition [3] have shown a significant performance improvement by reducing the problem's dimensionality while maintaining acceptable accuracy. For instance, in computational

---

\*Corresponding author.

*Email addresses:* [elena.benvenuti@unife.it](mailto:elena.benvenuti@unife.it) (Elena Benvenuti), [gmanzini@lanl.gov](mailto:gmanzini@lanl.gov) (Gianmarco Manzini), [marco.nale@unife.it](mailto:marco.nale@unife.it) (Marco Nale), [simone.pizzolato@edu.unife.it](mailto:simone.pizzolato@edu.unife.it) (Simone Pizzolato)

homogenization, a computational complexity of  $\mathcal{O}(N^d)$  is usually required, with  $N$  being the number of degrees of freedom in each spatial dimension (or a convenient upper bound of it) and  $d$  being the number of dimensions. This exponential scaling with  $d$  is called the *curse of dimensionality* [4], and is a major issue in the numerical resolution of high-dimensional problems.

The development of data compression techniques based on tensor-network formats, particularly the tensor train (TT) format [5, 6], has achieved a breakthrough in high-dimensional data compression, efficient numerical computations, and multi-dimensional array representation. The tensor train format, which emerged from intensive research [5, 7–9], offers an effective strategy for handling complex tensorial structures. This same mathematical framework, independently developed in quantum physics [10–13], is known as Matrix Product States (MPS) and serves as a fundamental tool for analyzing quantum spin systems.

The distinguishing characteristics of the TT framework make it exceptionally valuable for solving partial differential equations (PDEs). A key advantage lies in its storage efficiency: while traditional tensor representations face exponential growth in memory requirements with increasing dimensionality, the TT format achieves linear scaling in the number of separated dimensions, with only quadratic dependence on the ranks. Therefore, the computational complexity scales like  $\mathcal{O}(dr^2N)$  instead of  $\mathcal{O}(N^d)$ , where  $r$  is a suitable upper bound on the TT ranks, and it is significantly reduced whenever  $r \ll N$ , i.e., when a *low-rank approximation* is feasible. Additionally, it is worth emphasizing that a tensor train decomposition algorithm exists that enables the computation of “quasi-optimal” approximations of any given tensors through a systematic application of singular value decompositions on auxiliary matrices, see, e.g., [5, Alg. 1]. The interplay between the accuracy of such approximation and the computational costs can be controlled directly through a user-defined tolerance factor  $\epsilon$ .

The practical utility of the TT format in designing efficient and effective algorithms that approximate partial differential equations is enhanced by its compatibility with fundamental linear algebraic operations. The tensor train framework incorporates efficient mechanisms for these computations, complemented by robust rank reduction procedures, such as [11] and [5, Alg. 2], for managing the complexity of intermediate results. These features collectively establish the TT format as a powerful tool for tackling high-dimensional computational challenges. The mathematical foundation of this approach ensures both numerical stability and computational efficiency, making it particularly valuable for advanced scientific computing applications.

The *Quantized Tensor Train (QTT)* format [14] extends this approach by introducing the concept of “*quantization of tensor dimensions*”. Adopting the QTT format may lead to enhanced compression rates and efficiency, which is particularly effective in solving PDEs. Although this mathematical concept is relatively new in the field of low-rank representations, it has rapidly demonstrated its remarkable utility across numerical linear algebra and computational science applications. In fact, numerous discrete operators naturally exhibit low-rank structure when expressed in the QTT format, such as [15–20], and this characteristic proves fundamental in developing efficient tensor-based numerical approximations to PDE solutions. Furthermore, the QTT-FEM methodology, which integrates low-rank QTT decomposition with a fine-grained low-order finite element method, presents a robust framework for obtaining accurate solutions for multidimensional PDEs while maintaining computational efficiency. In the last decade, extensive research [14, 21–28]

has explored various partial differential models using this approach. Notably, investigations into elliptic PDEs featuring singularities or high-frequency oscillatory behaviors [14, 24–26, 29] have demonstrated exponential convergence rates relative to the total parameter count, achieving results comparable to those observed in hp-FEM applications for singular solutions. The framework’s effectiveness is further enhanced through advanced preconditioning strategies. The development of tensor-structured BPX preconditioners, initially proposed in [24] for uniformly elliptic problems and later extended to one-dimensional singularly perturbed scenarios [20] enables the practical implementation of low-rank QTT representations on extremely refined grids. This capability to handle grid resolutions approaching machine precision typically eliminates the need for adaptive mesh refinement procedures.

Recently published scientific literature focused on the application of QTT-based numerical methods across diverse PDE categories. Second-order elliptic PDEs have received significant attention [14, 20, 25, 26, 28–30] while specific investigations targeted the one-dimensional Helmholtz equation [25, 31], the chemical master equation [22, 32], the molecular Schrödinger equation [30], and Fokker-Planck equation [21]. The work we present in this paper has mainly been motivated by the work of Reference [28], where the application of the QTT format is explored within a FEM framework to solve the two-dimensional Poisson equation on polygonal domains. Our work extends the approach of References [28] to the linear elasticity model. As in [28], we highlight the potential of the QTT format to reduce memory consumption and to improve computational speed compared to traditional sparse matrix representations, particularly for fine meshes. Moreover, using QTT in a domain-splitting setting makes it possible to generalize the use of QTT format to computational domains with a more general geometric shape, as, for example, the “L-shape” that we consider in our numerical experiments. Achieving optimal performance in the domain-splitting framework demands a comprehensive redesign of how a finite element solver works, with special care to the mesh organizations, a different reordering of nodes and degrees of freedom, restructuring of stiffness matrix, and internal nodal force assembly procedures, and, finally, a reimplementaion of basic algebraic operations. A crucial point in keeping the possible rank growth under control is the adoption of a special renumbering of the degrees of freedom that follows the so-called *Z-order*, see [33, 34], and, accordingly, the introduction of Z-kron operations [28], enabling the construction of the stiffness matrix in Z-order directly in QTT format. The main contribution of our work relies on a thorough discussion of all the details and technicalities needed by the QTT-FEM and experimentally proving its effectiveness in solving the linear elasticity equation in variational form. Our main result is that the combined strengths of FEM’s adaptability to complex geometries, and QTT’s computational efficiency can significantly enhance the performance of numerical simulations, particularly in challenging scenarios involving singularities.

The paper is organized as follows. Section 2 introduces the mathematical formulation of the linear elasticity problem, discussing both its strong and weak forms. Section 3 presents the finite element formulation in a domain partitioning framework. Section 4 discusses a reformulation of the FEM by using the quantized tensor train format. Section 5 presents the result of our numerical experiments. Section 6 offers final remarks and some hints about possible future work.

## 2. The linear elasticity model

The linear elasticity model describes the small deformation behavior of an elastic material under external forces or displacements. We typically express the strong form of the linear elasticity problem through the equilibrium equation with appropriate boundary conditions.

First, let  $\Omega \subset \mathbb{R}^2$  be a two-dimensional domain occupied by an elastic body, and  $\partial\Omega$  its boundary, which can be divided into two disjoint parts:  $\partial\Omega_u$  where displacements are prescribed, and  $\partial\Omega_\sigma$  where tractions (stresses) are prescribed. Then, let  $\mathbf{u} = (u_s)_{s=1,2} \in \mathbb{R}^2$  be the displacement field and  $\varepsilon(\mathbf{u}) \in \mathbb{R}^{2 \times 2}$ , the strain, i.e., the symmetric gradient  $\varepsilon(\mathbf{u}) = \frac{1}{2}(\nabla\mathbf{u} + (\nabla\mathbf{u})^T)$ , where  $\nabla\mathbf{u} = (\partial u_s / \partial x_t)_{s,t=1,2}$ . Consider the stress tensor  $\sigma(\mathbf{u}) \in \mathbb{R}^{2 \times 2}$ , which is related to the strain tensor  $\varepsilon(\mathbf{u})$  by the constitutive (material) law, typically Hooke's law for linear elastic materials,  $\sigma(\mathbf{u}) = C : \varepsilon(\mathbf{u})$ , where  $C$  is the fourth-order elasticity tensor. The equilibrium equation is:

$$\nabla \cdot \sigma + \mathbf{f} = 0 \quad \text{in } \Omega, \quad (1)$$

where the vector-valued field  $\mathbf{f}$  represents the body forces. To properly define the mathematical model, we need the boundary conditions:

$$\mathbf{u} = \mathbf{u}_0 \quad \text{on } \partial\Omega_u, \quad (2a)$$

$$\sigma \cdot \mathbf{n} = \mathbf{t} \quad \text{on } \partial\Omega_\sigma, \quad (2b)$$

where  $\mathbf{u}_0$  in (2a) is a prescribed displacement on the Dirichlet boundary  $\partial\Omega_u$ ;  $\mathbf{t}$  in (2b) is the prescribed traction on the Neumann boundary  $\partial\Omega_\sigma$ ;  $\mathbf{n}$  in (2b) is the unit vector orthogonal to  $\partial\Omega_\sigma$  and pointing out of  $\Omega$ . We assume that the boundaries  $\partial\Omega_u$  and  $\partial\Omega_\sigma$  are nonoverlapping, in the sense that  $|\partial\Omega_u \cap \partial\Omega_\sigma| = 0$ , where  $|\cdot|$  is the one-dimensional Lebesgue measure of its argument.

As usual, we derive the weak form of problem (1)-(2) by multiplying (1) by a vector-valued test function  $\mathbf{v}$  that vanishes on  $\partial\Omega_u$ , and by integrating by parts over the domain  $\Omega$ . Using Hooke's law and noting that  $C$  is a major symmetric tensor, the variational form of the linear elasticity problem reads as:

*Find  $\mathbf{u} \in \mathbf{V}$  such that:*

$$a(\mathbf{u}, \mathbf{v}) := \int_{\Omega} \nabla\mathbf{u} : C : \nabla\mathbf{v} \, d\Omega = \int_{\Omega} \mathbf{f} \cdot \mathbf{v} \, d\Omega + \int_{\partial\Omega_\sigma} \mathbf{t} \cdot \mathbf{v} \, dS =: F(\mathbf{v}) \quad \forall \mathbf{v} \in \mathbf{V}_0, \quad (3)$$

with the affine space  $\mathbf{V} = \{\mathbf{v} \in [H^1(\Omega)]^2 : \mathbf{v} = \mathbf{u}_0 \text{ on } \partial\Omega_u\}$ , and the linear subspace  $\mathbf{V}_0$ , which is obtained by setting  $\mathbf{u}_0 = 0$  in  $\mathbf{V}$ . The well-posedness of the variational formulation (3) follows from an application of the Lax-Milgram theorem, which depends on the coercivity and continuity of the bilinear form  $a(\mathbf{u}, \mathbf{v})$ , and the continuity of the linear functional  $F(\mathbf{v})$ .

This equation states that for all admissible test functions  $\mathbf{v}$ , the internal virtual work done by the stresses must equal the external virtual work done by the body forces and tractions. The elasticity tensor  $C$  is a central component in the theory of linear elasticity, representing the material's response to mechanical stress. Such a tensor plays a crucial role in linking the stress tensor  $\sigma$  to the strain tensor  $\varepsilon$  through the Hooke's law, which in tensor form is expressed as:  $\sigma(\mathbf{u}) = C : \varepsilon(\mathbf{u})$ . For

isotropic materials, where properties are the same in all directions, the tensor  $C$  can be simplified significantly so that it is characterized by only two independent constants, usually chosen as the Young's modulus  $E$  and the Poisson's ratio  $\nu$ . The relationship, in this case, can be expressed as:

$$C_{ijkl} = \lambda \delta_{ij} \delta_{kl} + \mu (\delta_{ik} \delta_{jl} + \delta_{il} \delta_{jk}),$$

where  $\lambda$  and  $\mu$  are the Lamé constants, related to  $E$  and  $\nu$  by

$$\lambda = \frac{E\nu}{(1+\nu)(1-2\nu)}, \quad \mu = \frac{E}{2(1+\nu)}.$$

The elasticity tensor is also related to the potential energy stored in the material due to deformation. Finally, the strain energy density  $W$  for small deformations is given by:

$$W = \frac{1}{2} \varepsilon : C : \varepsilon.$$

This relation expresses how energy is distributed and stored in the material as a function of the strain, mediated by the properties encapsulated in  $C$ .

### 3. Finite element formulation

To simplify the presentation, we consider the case where the boundary of the domain associated with the stress variable,  $\partial\Omega_\sigma$ , is the empty set so that the boundary of the domain associated with the displacement variable,  $\partial\Omega_u$  coincides with the overall domain boundary,  $\partial\Omega$ . Additionally, we impose homogeneous Dirichlet boundary conditions by setting to zero  $\mathbf{u}_0$ , the prescribed displacement at the boundary  $\partial\Omega_u$ . Therefore, we solve the partial differential equation problem:

$$\nabla \cdot \sigma + \mathbf{f} = 0 \quad \text{in } \Omega, \tag{4a}$$

$$\mathbf{u} = 0 \quad \text{on } \partial\Omega. \tag{4b}$$

The corresponding weak form reads as

Find  $\mathbf{u} \in [H_0^1(\Omega)]^2$  such that:

$$\int_{\Omega} \sigma(\mathbf{u}) : \varepsilon(\mathbf{v}) \, d\Omega = \int_{\Omega} \mathbf{f} \cdot \mathbf{v} \, d\Omega \quad \forall \mathbf{v} \in [H_0^1(\Omega)]^2. \tag{5}$$

Extending this formulation to the more general formulation (3) of the previous section is straightforward, although requiring more technicalities.

To construct a finite element approximation of this problem that is suitable to the QTT methodology, we consider the *domain partitioning technique*, following the idea originally proposed in [28] for the Poisson equation. In practice, we split the open domain  $\Omega$  into a set of  $q$  open subdomains  $\Omega^{(m)}$  for  $m = 1, 2, \dots, q$ , and reformulate (5) on each subdomain. The regularity of the exact and approximate solutions implies that we can ignore the interface integral terms that appear from a subdomain integration by parts (a formal discussion about this point follows below). Then, we

assemble the global stiffness matrix and the global load term directly in the QTT format from the local stiffness matrices and load terms calculated on each subdomain, and we solve such a global problem through the AMEn solver [35]. Hereafter, we present the domain partitioning approach for the finite element discretization of (5); we will discuss the application of the QTT methodology in the next section.

It is worth noting that *our approach does not follow a domain decomposition strategy*, where we should solve the partial differential equation concurrently on each subdomain and reiterate after exchanging information between the subdomains across their common interfaces, see, cf. [36]. Nevertheless, a key point in this procedure is that the interface nodes, which are shared by two adjacent subdomains, are replicated in each subdomain in order to maintain  $2^d$  nodes per side partition as required by the QTT format. Therefore, we will need a set of additional equations in the final linear system to impose the numerical solution continuity at the shared interface nodes. This crucial point will be discussed in Section 3.3.1.

### 3.1. Domain partitioning approach

We partition the open domain  $\Omega$  into  $q$  open, quadrangular subdomains  $\Omega^{(m)}$  with boundary  $\partial\Omega^{(m)}$ , for  $m = 1, 2, \dots, q$ , such that

$$\bar{\Omega} = \bigcup_{m=1}^q \bar{\Omega}^{(m)},$$

where  $\bar{\Omega}$  and  $\bar{\Omega}^{(m)}$  denote the closure in  $\mathbb{R}^2$  of  $\Omega$  and  $\Omega^{(m)}$ , respectively. We split the boundary of the  $m$ -th subdomain as  $\partial\Omega^{(m)} = \Gamma^{(m,\text{ext})} \cup \Gamma^{(m,\text{int})}$ , where  $\Gamma^{(m,\text{ext})} := \partial\Omega \cap \partial\Omega^{(m)}$  lies on the external boundary  $\partial\Omega$ , and  $\Gamma^{(m,\text{int})} := \partial\Omega^{(m)} \setminus \Gamma^{(m,\text{ext})}$  is the internal boundary, which has to be shared with at least another subdomain. From this definition, it trivially follows that the sub-boundaries  $\Gamma^{(m,\text{ext})}$  and  $\Gamma^{(m,\text{int})}$  are non-overlapping. They can share mesh nodes, but they must also satisfy the condition that  $|\Gamma^{(m,\text{ext})} \cap \Gamma^{(m,\text{int})}| = 0$ , where  $|\mathfrak{s}|$  is the one-dimensional Lebesgue measure in  $\mathbb{R}^2$  of set  $\mathfrak{s}$  (the length of  $\mathfrak{s}$ ). To ease the notation, we will use the symbol  $\Gamma^{(m)}$  instead of  $\Gamma^{(m,\text{int})}$  to denote the internal boundary of a single domain  $\Omega^{(m)}$ . Similarly, we will use the symbol  $\Gamma^{(m|p)} = \partial\Omega^{(m)} \cap \partial\Omega^{(p)}$  to denote the interface specifically shared by the two subdomains  $\Omega^{(m)}$  and  $\Omega^{(p)}$  (with  $m \neq p$ ).

After splitting the domain  $\Omega$  into a set of  $m$  disjoint sub-domains  $\Omega^{(m)}$ , we consider a finite element approximation of the partial differential equation

$$-\nabla \cdot (C : \nabla \mathbf{u}^{(m)}) = \mathbf{f}^{(m)} \quad \text{in } \Omega^{(m)}, \quad (6)$$

$$\mathbf{u}^{(m)} = 0 \quad \text{on } \Gamma^{(m,\text{ext})}, \quad (7)$$

where  $\mathbf{u}^{(m)} = \mathbf{u}|_{\Omega^{(m)}}$ ,  $\mathbf{f}^{(m)} = \mathbf{f}|_{\Omega^{(m)}}$ , and assuming that the flux vector  $\mathbf{n} \cdot \sigma(\mathbf{u})$  is continuous at every internal interface. This continuity condition is consistent with the regularity assumption that  $\mathbf{u}$  belongs to  $[H_0^1(\Omega)]^2$ . Indeed, to derive the weak form of (6)-(7) on each subdomain  $\Omega^{(m)}$ , we multiply both sides of (6) by the vector-valued test function  $\mathbf{v} \in [H_0^1(\Omega)]^2$ , integrate by parts over

$\Omega^{(m)}$  and add the resulting expression over all the subdomains, so for  $m = 1, 2, \dots, q$ . We remove the external boundary integrals using (7). Then, let  $\Omega^{m^+}$  and  $\Omega^{m^-}$  be two subdomains sharing a common interface  $\Gamma^{(m^+|m^-)} \supseteq \partial\Omega^{m^+} \cap \partial\Omega^{m^-}$ . We introduce the jump operator at  $\Gamma^{(m^+|m^-)}$  that is defined as

$$\llbracket C : \nabla \mathbf{u} \rrbracket_{\Gamma^{(m^+|m^-)}} = [\mathbf{n} \cdot (C : \nabla \mathbf{u})]^+ + [\mathbf{n} \cdot (C : \nabla \mathbf{u})]^-,$$

where the superscripts  $\pm$  now indicate the side of the  $\Gamma$ -interface on which the trace of the normal flux  $\mathbf{n} \cdot (C : \nabla \mathbf{u})$  is taken. After the integration by parts, we renumber all interfaces as  $\Gamma^{(s)}$ , with  $s$  ranging from 1 to the total number of interfaces. Finally, we rearrange the interface summation term  $\left[ \sum_{m=1}^q \int_{\Gamma^{(m)}} \dots \right]$  as a summation over all the subdomain interfaces, e.g.,  $\left[ \sum_s \int_{\Gamma^{(s)}} \dots \right]$ , and we obtain:

$$\begin{aligned} & \sum_{m=1}^q \left( \int_{\Omega^{(m)}} \nabla \mathbf{u}^{(m)} : C : \nabla \mathbf{v} \, d\Omega - \int_{\Gamma^{(m)}} (\mathbf{n} \cdot (C : \nabla \mathbf{u})) \mathbf{v} \, dS \right) \\ &= \sum_{m=1}^q \int_{\Omega^{(m)}} \nabla \mathbf{u}^{(m)} : C : \nabla \mathbf{v} \, d\Omega - \sum_s \int_{\Gamma^{(s)}} \llbracket C : \nabla \mathbf{u} \rrbracket_{\Gamma^{(s)}} \mathbf{v} \, dS \\ &= \int_{\Omega} \nabla \mathbf{u}^{(m)} : C : \nabla \mathbf{v} \, d\Omega. \end{aligned} \quad (8)$$

The final equality in (8) is achieved since the continuity of the flux implies that  $\llbracket C : \nabla \mathbf{u} \rrbracket_{\Gamma^{(s)}} = 0$ .

### 3.2. Canonical and Z-ordering of the degrees of freedom

To define the finite element approximation in the subdomain  $\Omega^{(m)}$ , it is essential to establish a mapping between the nodal variables and a linear indexing system. Specifically, let  $\Omega_h^{(m)}$  be the mesh partitioning of the subdomain  $\Omega^{(m)}$ , built as the tensor product of univariate partitions with  $n = 2^d$  nodes per side. We can identify every mesh node of  $\Omega_h^{(m)}$  with the index pair  $(i, j)$ ,  $i, j = 0, \dots, 2^d - 1$ , and label each node with a single index  $\mathcal{L}_{ij} = i + 2^d j$ , ranging from 0 to  $4^d - 1$ . We will refer to  $\mathcal{L}_{ij}$  as the *canonical order* of the nodes  $\Omega^{(m)}$ .

We will also consider a different enumeration called the *Z-order*. This different numbering system identifies the  $(i, j)$ -th mesh node with the number  $\mathcal{Z}_{ij}$ , which we uniquely determine by interleaving the binary representation of indices  $i$  and  $j$ , see [34]. Hence, we first expand  $i$  and  $j$  on a binary digit format  $[\dots]_2$ ,

$$i = \sum_{k=1}^d 2^{k-1} i_k \leftrightarrow i \equiv [i_1, i_2, \dots, i_d]_2 \quad \text{and} \quad j = \sum_{k=1}^d 2^{k-1} j_k \leftrightarrow j \equiv [j_1, j_2, \dots, j_d]_2,$$

where  $i_d$  and  $j_d$  are the most significant digits of  $i$  and  $j$ , respectively. Then, we compute

$$\begin{aligned} \mathcal{Z}_{ij} &= i_1 + 2j_1 + 4i_2 + 8j_2 + \dots + 2^{2d-2} i_d + 2^{2d-1} j_d = \sum_{k=1}^d 2^{2k-2} i_k + \sum_{k=1}^d 2^{2k-1} j_k \\ &\leftrightarrow \mathcal{Z}_{ij} \equiv [i_1, j_1, i_2, j_2, \dots, i_d, j_d]_2. \end{aligned}$$

In the case of scalar fields, every mesh node is associated with a nodal value, and, thus, with the number  $\mathcal{L}_{ij}$  or  $\mathcal{Z}_{ij}$ . In the context of two-dimensional vector fields, we have two nodal values associated with every mesh node, e.g.,  $\mathbf{u}(x_i, y_j) = (u_x(x_i, y_j), u_y(x_i, y_j))^T$  for the node with coordinates  $(x_i, y_j)$ . Consequently, we introduce a two-dimensional enumeration of the nodal degrees of freedom for the canonical order,

$$\mathcal{N}_{ij} = \begin{bmatrix} \mathcal{N}_{ij}^x \\ \mathcal{N}_{ij}^y \end{bmatrix} = \begin{bmatrix} 2\mathcal{L}_{ij} + 1 \\ 2\mathcal{L}_{ij} + 2 \end{bmatrix},$$

and for the Z-order,

$$\mathcal{P}_{ij} = \begin{bmatrix} \mathcal{P}_{ij}^x \\ \mathcal{P}_{ij}^y \end{bmatrix} = \begin{bmatrix} 2\mathcal{Z}_{ij} + 1 \\ 2\mathcal{Z}_{ij} + 2 \end{bmatrix}.$$

### 3.3. Finite element approximation on subdomain $\Omega^{(m)}$

For exposition's sake, we use hereafter the canonical order using  $\mathcal{L}_{ij}$  and  $\mathcal{N}_{ij}$ . Switching to the Z-order formulation is almost straightforward and implies using  $\mathcal{Z}_{ij}$  and  $\mathcal{P}_{ij}$  instead of  $\mathcal{L}_{ij}$  and  $\mathcal{N}_{ij}$  in the following formula derivations.

On every subdomain  $\Omega^{(m)}$ , we consider the finite element approximation of the displacement vector field  $\mathbf{u}^{(m)}$ , which is given by:

$$\mathbf{u}^{(m)}(x, y) \approx \sum_{i,j=1}^{2^d} \phi_{\mathcal{L}_{ij}}^{(m)}(x, y) \mathbf{U}_{\mathcal{N}_{ij}}^{(m)},$$

where  $\phi_{\mathcal{L}_{ij}}^{(m)}(x, y)$  is the finite element shape function associated with the local mesh node  $\mathcal{L}_{ij}$ , and the vector coefficients  $\mathbf{U}_{\mathcal{N}_{ij}}^{(m)}$  denotes the degrees of freedom associated with such a node.

We use the Lagrangian isoparametric elements; hence, the shape function  $\phi_{\mathcal{L}_{ij}}^{(m)}$  is the piecewise bilinear function that is one at node  $\mathcal{L}_{ij}$  and zero at all other nodes within  $\Omega_h^{(m)}$ . We refer to [37] for details on the approximation properties of this discretization. The displacement vector components in the  $x$  and  $y$  directions are expressed as:

$$u_x^{(m)}(x, y) = \sum_{i,j=1}^{2^d} \phi_{\mathcal{L}_{ij}}^{(m)}(x, y) U_{\mathcal{N}_{ij}^x}^{(m)} \quad \text{and} \quad u_y^{(m)}(x, y) = \sum_{i,j=1}^{2^d} \phi_{\mathcal{L}_{ij}}^{(m)}(x, y) U_{\mathcal{N}_{ij}^y}^{(m)}.$$

The array  $\mathbf{U}^{(m)}$  holds the nodal unknowns and is organized as:

$$\mathbf{U}^{(m)} = \left( U_{\mathcal{N}_{ij}^x}^{(m)}, U_{\mathcal{N}_{ij}^y}^{(m)} \right)^T.$$

This leads to the local linear system:

$$\mathbf{K}^{(m)} \mathbf{U}^{(m)} + [\text{interface terms}] = \mathbf{f}^{(m)},$$



where  $\mathbf{f}^{(m)} = \left( f_{\mathcal{N}_{ij}^x}^{(m)}, f_{\mathcal{N}_{ij}^y}^{(m)} \right)^T$  is the vector of nodal forces, defined by the subdomain integrals:

$$f_{\mathcal{N}_{ij}^x}^{(m)} = \int_{\Omega^{(m)}} f_x \phi_{\mathcal{L}_{ij}}^{(m)} dx dy \quad \text{and} \quad f_{\mathcal{N}_{ij}^y}^{(m)} = \int_{\Omega^{(m)}} f_y \phi_{\mathcal{L}_{ij}}^{(m)} dx dy,$$

and  $\mathbf{K}^{(m)}$  represents the stiffness matrix that is detailed in the next subsections. We left the interface terms unspecified because they add to zero when we assemble the global linear system as proved in (8).

### 3.3.1. Solution concatenation

We extend the procedure proposed by Markeeva et al. [28] to impose a compatibility constraint between the solutions of the system of equations on the subdomains to the vector case. Each subdomain is a quadrangle meshed with  $2^d \times 2^d$  nodes. Let  $i, j \in [1 \dots 2^d]$  indicate the position of the generic  $(i, j)$ -th node in the mesh. In the two-dimensional elasticity vector case, we need to introduce the multi-index  $\mathcal{N}_{ij}$  collecting the local index numbers in  $x$  and  $y$ , i.e.,  $\mathcal{N}_{ij}^x$  and  $\mathcal{N}_{ij}^y$ . Then, by using this notation and omitting the interface terms, we can rewrite the local linear system of equations at node  $\mathcal{N}_{ij}$  as:

$$\sum_{k,l=1}^{2^d} \mathbf{K}_{\mathcal{N}_{ij}, \mathcal{N}_{kl}}^{(m)} \mathbf{U}_{\mathcal{N}_{kl}}^{(m)} = \mathbf{f}_{\mathcal{N}_{ij}}^{(m)}. \quad (9)$$

When a node is located at the crossroad among  $N_s$  subdomains, the equilibrium equation (9) can be rewritten taking into account the additive contribution of these subdomains as follows:

$$\sum_{s=1}^{N_s} \sum_{k,l=1}^{2^d} \mathbf{K}_{\mathcal{N}_{ij}, \mathcal{N}_{kl}}^{(s)} \mathbf{U}_{\mathcal{N}_{kl}}^{(s)} = \sum_{s=1}^{N_s} \mathbf{f}_{\mathcal{N}_{ij}}^{(s)}. \quad (10)$$

For example, let subdomains  $m_1$  and  $m_2$  share a side, and assume that the node  $(i_1, j_1)$  from  $m_1$  coincide with the node  $(i_2, j_2)$  from  $m_2$ . The compatibility between the displacement at the junction node is restored by imposing the following conditions:

$$\mathbf{U}_{\mathcal{N}_{i_1 j_1}^x}^{(m_1)} = \mathbf{U}_{\mathcal{N}_{i_2 j_2}^x}^{(m_2)} \quad (11a)$$

$$\mathbf{U}_{\mathcal{N}_{i_1 j_1}^y}^{(m_1)} = \mathbf{U}_{\mathcal{N}_{i_2 j_2}^y}^{(m_2)}. \quad (11b)$$

Then, conditions (11a) are satisfied via a Lagrangian multiplier approach as follows:

$$\begin{aligned}
\lambda(\mathbf{U}_{\mathcal{N}_{i_1 j_1}^x}^{(m_1)} - \mathbf{U}_{\mathcal{N}_{i_2 j_2}^x}^{(m_2)}) + \sum_{k,l=1}^{2^d} \mathbf{K}_{\mathcal{N}_{i_1 j_1}, \mathcal{N}_{kl}}^{(m_1)} \mathbf{U}_{\mathcal{N}_{kl}}^{(m_1)} + \sum_{k,l=1}^{2^d} \mathbf{K}_{\mathcal{N}_{i_2 j_2}, \mathcal{N}_{kl}}^{(m_2)} \mathbf{U}_{\mathcal{N}_{kl}}^{(m_2)} &= \mathbf{f}_{\mathcal{N}_{i_1 j_1}}^{(m_1)} + \mathbf{f}_{\mathcal{N}_{i_2 j_2}}^{(m_2)}, \\
\lambda(\mathbf{U}_{\mathcal{N}_{i_1 j_1}^y}^{(m_1)} - \mathbf{U}_{\mathcal{N}_{i_2 j_2}^y}^{(m_2)}) + \sum_{k,l=1}^{2^d} \mathbf{K}_{\mathcal{N}_{i_1 j_1}, \mathcal{N}_{kl}}^{(m_1)} \mathbf{U}_{\mathcal{N}_{kl}}^{(m_1)} + \sum_{k,l=1}^{2^d} \mathbf{K}_{\mathcal{N}_{i_2 j_2}, \mathcal{N}_{kl}}^{(m_2)} \mathbf{U}_{\mathcal{N}_{kl}}^{(m_2)} &= \mathbf{f}_{\mathcal{N}_{i_1 j_1}}^{(m_1)} + \mathbf{f}_{\mathcal{N}_{i_2 j_2}}^{(m_2)} \mathbf{U}_{\mathcal{N}_{kl}}^{(m_2)}, \\
\lambda(\mathbf{U}_{\mathcal{N}_{i_2 j_2}^x}^{(m_2)} - \mathbf{U}_{\mathcal{N}_{i_1 j_1}^x}^{(m_1)}) + \sum_{k,l=1}^{2^d} \mathbf{K}_{\mathcal{N}_{i_1 j_1}, \mathcal{N}_{kl}}^{(m_1)} \mathbf{U}_{\mathcal{N}_{kl}}^{(m_1)} + \sum_{k,l=1}^{2^d} \mathbf{K}_{\mathcal{N}_{i_2 j_2}, \mathcal{N}_{kl}}^{(m_2)} \mathbf{U}_{\mathcal{N}_{kl}}^{(m_2)} &= \mathbf{f}_{\mathcal{N}_{i_1 j_1}}^{(m_1)} + \mathbf{f}_{\mathcal{N}_{i_2 j_2}}^{(m_2)}, \\
\lambda(\mathbf{U}_{\mathcal{N}_{i_2 j_2}^y}^{(m_2)} - \mathbf{U}_{\mathcal{N}_{i_1 j_1}^y}^{(m_1)}) + \sum_{k,l=1}^{2^d} \mathbf{K}_{\mathcal{N}_{i_1 j_1}, \mathcal{N}_{kl}}^{(m_1)} \mathbf{U}_{\mathcal{N}_{kl}}^{(m_1)} + \sum_{k,l=1}^{2^d} \mathbf{K}_{\mathcal{N}_{i_2 j_2}, \mathcal{N}_{kl}}^{(m_2)} \mathbf{U}_{\mathcal{N}_{kl}}^{(m_2)} &= \mathbf{f}_{\mathcal{N}_{i_1 j_1}}^{(m_1)} + \mathbf{f}_{\mathcal{N}_{i_2 j_2}}^{(m_2)},
\end{aligned}$$

where the Lagrangian multiplier  $\lambda$  is a positive real number.

### 3.3.2. Construction of the stiffness matrix

We obtain the stiffness matrix  $\mathbf{K}^{(m)} = \left( \mathbf{K}_{\mathcal{N}_{ij}\mathcal{N}_{kl}}^{(m)} \right)_{\mathcal{N}_{ij}, \mathcal{N}_{kl}=1,2,\dots,4^d}$  from the weak formulation by restricting the integration from  $\Omega$  in the bilinear form  $a(\mathbf{u}, \mathbf{v})$  to the subdomain  $\Omega^{(m)}$ . The components associated with the connected nodes  $\mathcal{L}_{ij}$  and  $\mathcal{L}_{kl}$  is:

$$\mathbf{K}_{\mathcal{N}_{ij}\mathcal{N}_{kl}}^{(m)} = \int_{\Omega^{(m)}} \mathbf{B}_{\mathcal{L}_{ij}}^T \mathbf{C} \mathbf{B}_{\mathcal{L}_{kl}} dx dy, \quad (12)$$

where  $\mathbf{C}$  is the constant, constitutive, symmetric matrix, which for the plane isotropic case is:

$$\mathbf{C} = \begin{bmatrix} C_{11} & C_{12} & 0 \\ C_{12} & C_{22} & 0 \\ 0 & 0 & C_{33} \end{bmatrix}, \quad (13)$$

and  $\mathbf{B}_{\mathcal{L}_{ij}}$  is the compatibility operator at the local node  $(x_i, y_j)$  that can be derived from the strain-displacement relationship  $\varepsilon_{\mathcal{L}_{ij}} = \mathbf{B}_{\mathcal{L}_{ij}} \mathbf{U}_{\mathcal{N}_{ij}}$ . Recalling that  $\mathbf{U}_{\mathcal{N}_{ij}} = (U_{\mathcal{N}_{ij}^x}, U_{\mathcal{N}_{ij}^y})^T$ , it holds that

$$\varepsilon(\mathbf{u}^{(m)}) = \begin{bmatrix} \varepsilon_{xx}(\mathbf{u}^{(m)}) \\ \varepsilon_{yy}(\mathbf{u}^{(m)}) \\ 2\varepsilon_{xy}(\mathbf{u}^{(m)}) \end{bmatrix} = \begin{bmatrix} \frac{\partial u_x^{(m)}}{\partial x} \\ \frac{\partial u_y^{(m)}}{\partial y} \\ \frac{\partial u_x^{(m)}}{\partial y} + \frac{\partial u_y^{(m)}}{\partial x} \end{bmatrix} \quad \text{and} \quad \mathbf{B}_{\mathcal{L}_{ij}} = \begin{bmatrix} \frac{\partial \phi_{\mathcal{L}_{ij}}^{(m)}}{\partial x} & 0 \\ 0 & \frac{\partial \phi_{\mathcal{L}_{ij}}^{(m)}}{\partial y} \\ \frac{\partial \phi_{\mathcal{L}_{ij}}^{(m)}}{\partial y} & \frac{\partial \phi_{\mathcal{L}_{ij}}^{(m)}}{\partial x} \end{bmatrix}, \quad (14)$$

where we adopted the Voigt notation (as usual in finite element discretization of elliptic problems [37]). Replacing (14) and (13) in (12), we recast the latter as:

$$\mathbf{K}_{\mathcal{N}_{ij}\mathcal{N}_{kl}}^{(m)} = \int_{\Omega^{(m)}} \begin{bmatrix} \frac{\partial \phi_{\mathcal{L}_{ij}}^{(m)}}{\partial x} & 0 & \frac{\partial \phi_{\mathcal{L}_{ij}}^{(m)}}{\partial y} \\ 0 & \frac{\partial \phi_{\mathcal{L}_{ij}}^{(m)}}{\partial y} & \frac{\partial \phi_{\mathcal{L}_{ij}}^{(m)}}{\partial x} \end{bmatrix} \begin{bmatrix} C_{11} & C_{12} & 0 \\ C_{12} & C_{22} & 0 \\ 0 & 0 & C_{33} \end{bmatrix} \begin{bmatrix} \frac{\partial \phi_{\mathcal{L}_{hk}}^{(m)}}{\partial x} & 0 \\ 0 & \frac{\partial \phi_{\mathcal{L}_{hk}}^{(m)}}{\partial y} \\ \frac{\partial \phi_{\mathcal{L}_{hk}}^{(m)}}{\partial y} & \frac{\partial \phi_{\mathcal{L}_{hk}}^{(m)}}{\partial x} \end{bmatrix} dx dy, \quad (15)$$

from which the following subdomain matrix descends:

$$\mathbf{K}_{\mathcal{N}_{ij}\mathcal{N}_{hk}}^{(m)} = \int_{\Omega} \begin{bmatrix} A_{\mathcal{N}_{ij}^x \mathcal{N}_{hk}^x}^{(m)} & A_{\mathcal{N}_{ij}^x \mathcal{N}_{hk}^y}^{(m)} \\ A_{\mathcal{N}_{ij}^y \mathcal{N}_{hk}^x}^{(m)} & A_{\mathcal{N}_{ij}^y \mathcal{N}_{hk}^y}^{(m)} \end{bmatrix} dx dy. \quad (16)$$

### 3.4. Subdomain numerical integration

We remap each element of the subdomain mesh  $\Omega_h^{(m)}$  onto the adimensional reference element  $\mathbb{K} = [-1, 1] \times [-1, 1]$  by introducing a bijective mapping from the global coordinate system  $(x, y)$  to the dimensionless coordinate system  $(\xi, \eta)$  defined on  $\mathbb{K}$ . Since we use the Lagrangian isoparametric elements, we consider the four shape functions associated with the corners of  $\mathbb{K}$ , which are

$$\begin{aligned} \Phi_{-1,-1}(\xi, \eta) &= \frac{(1-\xi)(1-\eta)}{4}, & \Phi_{1,-1}(\xi, \eta) &= \frac{(1+\xi)(1-\eta)}{4}, \\ \Phi_{1,1}(\xi, \eta) &= \frac{(1+\xi)(1+\eta)}{4}, & \Phi_{-1,1}(\xi, \eta) &= \frac{(1-\xi)(1+\eta)}{4}. \end{aligned}$$

Let  $(x_1, y_1), (x_2, y_2), (x_3, y_3), (x_4, y_4)$  be the coordinates of the four vertices of a given element of  $\Omega_h^{(m)}$ , which are respectively mapped onto the four vertices of  $\mathbb{K}$  with coordinates  $(-1, -1), (1, -1), (1, 1), (-1, 1)$ . To ease the notation, in this subsection we prefer dropping the superindex  $(m)$ , so that we denote the coordinate mappings as  $(x_\ell, y_\ell)$  instead of  $(x_\ell^{(m)}, y_\ell^{(m)})$  for  $\ell = 1, 2, 3, 4$ . We similarly remove the superindex  $(\cdot)$  in all quantities related to such mappings, e.g., their partial derivatives and Jacobian matrices. The change of coordinates is given by

$$\begin{bmatrix} x(\xi, \eta) \\ y(\xi, \eta) \end{bmatrix} = \begin{bmatrix} x_1 & x_2 & x_3 & x_4 \\ y_1 & y_2 & y_3 & y_4 \end{bmatrix} \begin{bmatrix} \Phi_{-1,-1}(\xi, \eta) \\ \Phi_{1,-1}(\xi, \eta) \\ \Phi_{1,1}(\xi, \eta) \\ \Phi_{-1,1}(\xi, \eta) \end{bmatrix},$$

so that  $(x(-1, 1), y(-1, 1)) = (x_1, y_1)$ , etc. The Jacobian matrix  $\mathbf{J}(\xi, \eta)$  of the transformation from  $(\xi, \eta)$  to  $(x, y)$  is non-singular. Therefore, the inverse Jacobian matrix  $\mathbf{J}^{-1}(x, y)$  associated with the

inverse mapping  $(\xi(x, y), \eta(x, y))$  from the reference element  $\mathbb{K}$  to a given mesh element of  $\Omega_h^{(m)}$  is also defined (and non-singular). The Jacobian matrix and its inverse take the form:

$$\mathbf{J}(\xi, \eta) = \begin{bmatrix} \frac{\partial x}{\partial \xi} & \frac{\partial y}{\partial \xi} \\ \frac{\partial x}{\partial \eta} & \frac{\partial y}{\partial \eta} \end{bmatrix}, \quad \mathbf{J}^{-1}(\xi, \eta) = \frac{1}{|\mathbf{J}(\xi, \eta)|} \begin{bmatrix} \frac{\partial \xi}{\partial x} & \frac{\partial \eta}{\partial x} \\ \frac{\partial \xi}{\partial y} & \frac{\partial \eta}{\partial y} \end{bmatrix},$$

where  $|\mathbf{J}(\xi, \eta)|$  is the determinant of  $\mathbf{J}(\xi, \eta)$ .

Let  $c \in \{(-1, -1), (-1, 1), (1, 1), (-1, 2)\}$  be a corner of the reference element and  $\Phi_c$  be the corresponding shape function. Then, consider a node  $\mathcal{L}_{ij}$  of the subdomain mesh  $\Omega_h^{(m)}$  and let  $c$  be the corresponding node of  $\mathbb{K}$  determined by the above mapping from a mesh element having the node  $\mathcal{L}_{ij}$  as one of its nodes to the adimensional coordinate system  $(\xi, \eta)$ . Let  $\mathbf{B}_c$  be the compatibility matrix  $\mathbf{B}_{\mathcal{L}_{ij}}$  at the node  $\mathcal{L}_{ij}$  that is mapped to  $c$  in  $\mathbb{K}$  expressed in the reference coordinate system  $(\xi, \eta)$ . On applying the coordinate transformation, we find that

$$\begin{aligned} \mathbf{B}_c &= \begin{bmatrix} \frac{\partial \Phi_c}{\partial \xi} \frac{\partial \xi}{\partial x} + \frac{\partial \Phi_c}{\partial \eta} \frac{\partial \eta}{\partial x} & 0 \\ 0 & \frac{\partial \Phi_c}{\partial \xi} \frac{\partial \xi}{\partial y} + \frac{\partial \Phi_c}{\partial \eta} \frac{\partial \eta}{\partial y} \\ \frac{\partial \Phi_c}{\partial \xi} \frac{\partial \xi}{\partial y} + \frac{\partial \Phi_c}{\partial \eta} \frac{\partial \eta}{\partial y} & \frac{\partial \Phi_c}{\partial \xi} \frac{\partial \xi}{\partial x} + \frac{\partial \Phi_c}{\partial \eta} \frac{\partial \eta}{\partial x} \end{bmatrix} = \begin{pmatrix} \frac{\partial \Phi_c}{\partial \xi}, \frac{\partial \Phi_c}{\partial \eta} \end{pmatrix} \begin{bmatrix} \begin{pmatrix} \frac{\partial \xi}{\partial x}, \frac{\partial \eta}{\partial x} \end{pmatrix}^T & 0 \\ 0 & \begin{pmatrix} \frac{\partial \xi}{\partial y}, \frac{\partial \eta}{\partial y} \end{pmatrix}^T \\ \begin{pmatrix} \frac{\partial \xi}{\partial y}, \frac{\partial \eta}{\partial y} \end{pmatrix}^T & \begin{pmatrix} \frac{\partial \xi}{\partial x}, \frac{\partial \eta}{\partial x} \end{pmatrix}^T \end{bmatrix} \\ &= \nabla_{\xi, \eta} \Phi_c(\xi, \eta) \widehat{\mathbf{J}}(x(\xi, \eta), y(\xi, \eta)), \end{aligned}$$

where we have set

$$\widehat{\mathbf{J}}(x(\xi, \eta), y(\xi, \eta)) := \begin{bmatrix} \begin{pmatrix} \frac{\partial \xi}{\partial x}, \frac{\partial \eta}{\partial x} \end{pmatrix}^T & 0 \\ 0 & \begin{pmatrix} \frac{\partial \xi}{\partial y}, \frac{\partial \eta}{\partial y} \end{pmatrix}^T \\ \begin{pmatrix} \frac{\partial \xi}{\partial y}, \frac{\partial \eta}{\partial y} \end{pmatrix}^T & \begin{pmatrix} \frac{\partial \xi}{\partial x}, \frac{\partial \eta}{\partial x} \end{pmatrix}^T \end{bmatrix}. \quad (17)$$

The last equality above implicitly defines the matrix  $\widehat{\mathbf{J}}$  that depends on the entries of  $\mathbf{J}^{-1}$ , i.e., on the derivatives of  $\xi(x, y)$  and  $\eta(x, y)$  with respect to  $x$  and  $y$ . To ease the notation, let use  $\widehat{\mathbf{J}}(\xi, \eta)$  to denote  $\widehat{\mathbf{J}}(x(\xi, \eta), y(\xi, \eta))$ . The contribution to the stiffness matrix from the pair of shape

functions  $\Phi_{c_1}$  and  $\Phi_{c_2}$  for  $c_1, c_2 \in \{(-1, -1), (-1, 1), (1, 1), (1, -1)\}$  is

$$\begin{aligned} \mathbf{K}_{c_1, c_2} &= \int_{\mathbb{K}} \mathbf{B}_{c_1}^T(\xi, \eta) \mathbf{C} \mathbf{B}_{c_2}(\xi, \eta) |\mathbf{J}_{\xi\eta}| d\xi d\eta \\ &= \int_{\mathbb{K}} \left[ \widehat{\mathbf{J}}^T(\xi, \eta) \left( \nabla_{\xi, \eta} \Phi_{c_1}(\xi, \eta) \right)^T \right] \mathbf{C} \left[ \nabla_{\xi, \eta} \Phi_{c_2}(\xi, \eta) \widehat{\mathbf{J}}(\xi, \eta) \right] |\mathbf{J}_{\xi\eta}| d\xi d\eta. \end{aligned} \quad (18)$$

The associated elastic energy is written as:

$$E_{c_1, c_2} = \frac{1}{2} \mathbf{U}_{c_1}^T \mathbf{K}_{c_1, c_2} \mathbf{U}_{c_2},$$

where we denote  $\mathbf{U}_{c_1} = (U_{c_1, x}, U_{c_1, y})^T$  and  $\mathbf{U}_{c_2} = (U_{c_2, x}, U_{c_2, y})^T$ , according to “c”-notation introduced above. To evaluate the stiffness matrix integrals, we consider a Gaussian quadrature rule that is obtained by the tensor product of the one-dimensional quadrature rules with same weights and node distributions  $\{(W_{g_i}, \xi_{g_i})\}$  and  $\{(W_{g_j}, \eta_{g_j})\}$  along the directions  $x$  and  $y$ , respectively. The numerical integration reads as:

$$\mathbf{K}_{c_1, c_2} \approx \sum_{g_i=1}^{N_{G_i}} \sum_{g_j=1}^{N_{G_j}} W_{g_i} W_{g_j} \mathbf{B}_{c_1}^T(\xi_{g_i}, \eta_{g_j}) \mathbf{C} \mathbf{B}_{c_2}(\xi_{g_i}, \eta_{g_j}) |\mathbf{J}(\xi_{g_i}, \eta_{g_j})|.$$

A further simplification is given by evaluating the integrand at the element center.

We can also approximate the partial derivatives of the Jacobian matrix in each mesh element of  $\Omega_h^{(m)}$  as follows. Consider the  $(i, j)$ -th element whose bottom-left corner is the mesh node identified by the index pair  $(i, j)$ , with  $i, j = 0, 1, \dots, 2^d - 1$ . We expand the entries of the Jacobian matrix in such an element, denoted by  $\mathbf{J}^{(i, j)}(\xi, \eta)$ , as follows:

$$\mathbf{J}^{(i, j)}(\xi, \eta) = \mathbf{J}^{(0, 0)}(\xi, \eta) + i(\mathbf{J}^{(1, 0)}(\xi, \eta) - \mathbf{J}^{(0, 0)}(\xi, \eta)) + j(\mathbf{J}^{(0, 1)}(\xi, \eta) - \mathbf{J}^{(0, 0)}(\xi, \eta)), \quad (19)$$

where  $\mathbf{J}^{(0, 0)}$ ,  $\mathbf{J}^{(1, 0)}$ , and  $\mathbf{J}^{(0, 1)}$  are the Jacobian matrices associated with the near elements that are identified by the index pairs  $(0, 0)$ ,  $(1, 0)$ ,  $(0, 1)$ , see Fig. 1. Using the Gauss nodes  $(\xi_{g_i}, \eta_{g_j})$ , we rewrite the formula above as:

$$\begin{aligned} \mathbf{J}^{(i, j)}(\xi_{g_i}, \eta_{g_j}) &= \mathbf{J}^{(0, 0)}(\xi_{g_i}, \eta_{g_j}) \\ &\quad + i(\mathbf{J}^{(1, 0)}(\xi_{g_i}, \eta_{g_j}) - \mathbf{J}^{(0, 0)}(\xi_{g_i}, \eta_{g_j})) + j(\mathbf{J}^{(0, 1)}(\xi_{g_i}, \eta_{g_j}) - \mathbf{J}^{(0, 0)}(\xi_{g_i}, \eta_{g_j})). \end{aligned}$$

Analogously, its determinant  $|\mathbf{J}^{(i, j)}(\xi, \eta)|$  is calculated using the expression:

$$|\mathbf{J}^{(i, j)}(\xi, \eta)| = |\mathbf{J}^{(0, 0)}(\xi, \eta)| + i|\mathbf{J}^{(1, 0)}(\xi, \eta) - \mathbf{J}^{(0, 0)}(\xi, \eta)| + j|\mathbf{J}^{(0, 1)}(\xi, \eta) - \mathbf{J}^{(0, 0)}(\xi, \eta)|. \quad (20)$$

Once  $\mathbf{J}^{(i, j)}$  is computed, the operator  $\widehat{\mathbf{J}}^{(i, j)}(\xi, \eta)$  is straightforwardly obtained from Eq. (17).

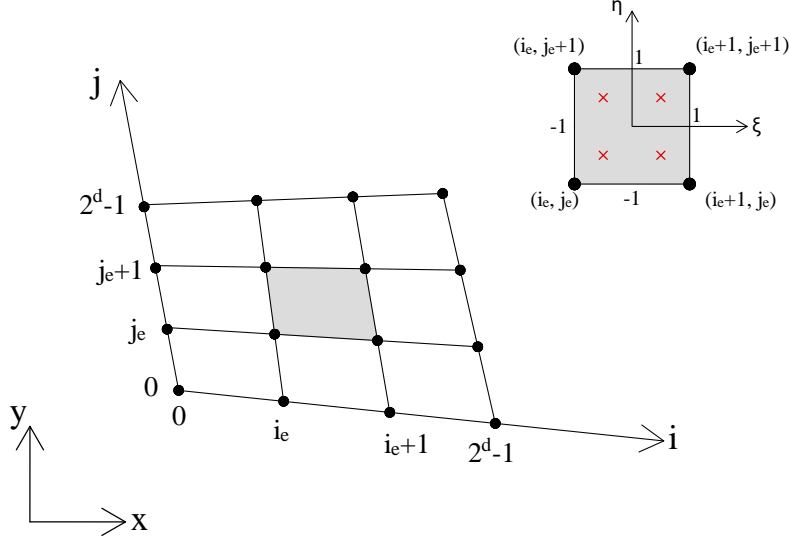


Figure 1: Mesh partition for the Jacobian calculation

### 3.5. Assembly at the subdomain level

All operations for computing  $\mathbf{K}_{c_1, c_2}$  for a given pair  $(c_1, c_2)$  are vectorizable; so, we can carry out the calculation for all the mesh elements of a particular domain, which are addressed by  $\mathcal{L}_{ij}$ , simultaneously. Let  $\mathcal{K}_{(c_1, c_2)}$  be the array collecting all the elemental integral values and  $\mathbf{V}_{c_1}$  and  $\mathbf{V}_{c_2}$  the shift matrices moving such values to their final position into the stiffness matrix  $\mathbf{K}_{(c_1, c_2)}^{(m)}$  associated with the subdomain  $\Omega^{(m)}$ . We formally write that

$$\mathbf{K}_{(c_1, c_2)}^{(m)} = \mathbf{V}_{c_1}^T \text{diag}(\mathcal{K}_{(c_1, c_2)}) \mathbf{V}_{c_2}, \quad (21)$$

and we obtain the stiffness matrix  $\mathbf{K}^{(m)}$  of  $\Omega^{(m)}$  by accumulating the contributions from all the sixteen possible pairs  $(c_1, c_2)$ , so that

$$\mathbf{K}^{(m)} = \sum_{(c_1, c_2)} \mathbf{K}_{(c_1, c_2)}^{(m)}. \quad (22)$$

We can build matrix  $\mathbf{K}^{(m)}$  in canonical or Z-order by a suitable choice of the shifting matrices  $\mathbf{V}_{c_1}$  and  $\mathbf{V}_{c_2}$ .

Analogously, for mesh element of  $\Omega_h^{(m)}$  and any one of the sixteen possible combinations of  $c_1$  and  $c_2$ , we compute the right-hand side load vector  $\mathbf{G}_{c_1, c_2}$  as

$$\mathbf{G}_{c_1, c_2} = \sum_{g_i=1}^{N_{G_i}} \sum_{g_j=1}^{N_{G_j}} W_{g_i} W_{g_j} \Phi_{c_1}(\xi_{g_i}, \eta_{g_j}) \Phi_{c_2}(\xi_{g_i}, \eta_{g_j}) |\mathbf{J}(\xi_{g_i}, \eta_{g_j})|$$

where  $\mathbf{J}_0$  is the Jacobian evaluated at the center of that mesh element. Then, we move the elemental values to their global position through the same shift matrices  $\mathbf{V}_{c_1}$  and  $\mathbf{V}_{c_2}$ , so that

$$\mathbf{f}_{c_1, c_2}^{(m)} = \mathbf{V}_{c_1}^T \text{diag}(\mathbf{G}_{c_1, c_2}) \mathbf{V}_{c_2} \bar{\mathbf{f}}, \quad (23)$$

where  $\bar{\mathbf{f}}$  denotes the force vector intensity. Finally, we consider the summation

$$\mathbf{f}^{(m)} = \sum_{(c_1, c_2)} \mathbf{f}_{c_1, c_2}^{(m)}, \quad (24)$$

which accumulates all contributions (23) on the right-hand side (RHS) load vector  $\mathbf{f}^{(m)}$ .

### 3.6. Assembly at the global domain level

We split the stiffness matrix  $\mathbf{K}^{(m)}$  and the RHS load vector  $\mathbf{f}^{(m)}$  of the subdomain  $\Omega^{(m)}$  as follows:

$$\mathbf{K}^{(m)} = \begin{bmatrix} \mathbf{K}_{xx}^{(m)} & \mathbf{K}_{xy}^{(m)} \\ \mathbf{K}_{yx}^{(m)} & \mathbf{K}_{yy}^{(m)} \end{bmatrix}, \quad \mathbf{f}^{(m)} = \begin{bmatrix} \mathbf{f}_x^{(m)} & \mathbf{f}_y^{(m)} \end{bmatrix}.$$

We introduce the compact notation  $\mathbf{K}_{\alpha\beta}^{(m)}$  and  $\mathbf{f}_\alpha^{(m)}$  where  $\alpha, \beta \in \{x, y\}$ . Then, we write each component  $(\alpha\beta)$  for the global domain  $\Omega$  by considering the contributions from all the  $q$  subdomains in this form

$$\mathbf{K}_{\alpha\beta} = \begin{bmatrix} \mathbf{K}_{\alpha\beta, 11} & \mathbf{K}_{\alpha\beta, 12} & \cdots & \mathbf{K}_{\alpha\beta, 1q} \\ \mathbf{K}_{\alpha\beta, 21} & \mathbf{K}_{\alpha\beta, 22} & \cdots & \mathbf{K}_{\alpha\beta, 2q} \\ \vdots & \vdots & \ddots & \vdots \\ \mathbf{K}_{\alpha\beta, q1} & \mathbf{K}_{\alpha\beta, q2} & \cdots & \mathbf{K}_{\alpha\beta, qq} \end{bmatrix}, \quad (25)$$

The block matrices  $\mathbf{K}_{\alpha\beta, mp}$  for  $m, p = 1, 2, \dots, q$  are originated by the subdomain concatenation through the common nodes that are shared at the internal interface.

#### 3.6.1. Subdomain concatenation

Following [28], a very efficient way to take such a concatenation into account is to introduce the connectivity matrix  $\mathbf{\Pi}^{(mp)}$  for every possible pair of subdomains labeled by  $m$  and  $p$ , whose  $(ij)$ -th component is defined as

$$(\mathbf{\Pi}^{(mp)})_{ij} = \begin{cases} 1 & \text{if } i^m \sim j^p, \\ 0 & \text{otherwise,} \end{cases}$$

where  $i^m \sim j^p$  means that the node  $i$  of the domain  $\Omega_h^{(m)}$  coincides with the node  $j^p$  of the domain  $\Omega_h^{(p)}$ . Let  $\gamma$  be a strictly positive, real number. We compute the diagonal terms of the matrix (25) as

$$\mathbf{K}_{\alpha\beta, mm} = \mathbf{K}_{\alpha\beta}^{(m)} - \gamma \mathbf{\Pi}^{(mm)},$$

and the extra-diagonal terms ( $m \neq p$ ) as

$$\mathbf{K}_{\alpha\beta,mp} = \begin{cases} \Pi^{(mp)} \mathbf{K}_{\alpha\beta}^{(p)} - \gamma \Pi^{(mp)} & \text{if } m \text{ and } p \text{ are adjacent,} \\ 0 & \text{otherwise.} \end{cases} \quad (26a)$$

A convenient value for  $\gamma$  is the mean value of the diagonal element of the stiffness matrix  $\mathbf{K}_{\alpha\beta}^{(m)}$ . Likewise, on employing the connectivity matrices defined above, we obtain the  $\alpha$ -component of the global RHS vector  $\mathbf{g}^{(m)}$  for  $\alpha \in \{x, y\}$  starting from the local force vector component  $\mathbf{f}_\alpha^{(m)}$  associated to the subdomain  $\Omega^{(m)}$ , which we write as follows:

$$\mathbf{g}_\alpha^{(m)} = \mathbf{f}_\alpha^{(m)} + \sum_{p \neq m} \Pi^{(mp)} \mathbf{f}^{(p)}. \quad (27)$$

In the above equation, the concatenation term takes into account the contribution from the other subdomains to the nodes of  $\Omega_h^{(m)}$  that are shared through the common internal interfaces.

### 3.7. Final stiffness matrix and force vector

According to the previous section, we compute the four global stiffness matrices  $\mathbf{K}_{xx}$ ,  $\mathbf{K}_{xy}$ ,  $\mathbf{K}_{yx}$ ,  $\mathbf{K}_{yy}$  and two global force vectors  $\mathbf{f}_x$  and  $\mathbf{f}_y$ . Finally, we compute the stiffness matrix  $\mathbf{K}$  and the force vector  $\mathbf{f}$  using the Kronecker product:

$$\mathbf{K} = \begin{bmatrix} 1 & 0 \\ 0 & 0 \end{bmatrix} \otimes \mathbf{K}_{xx} + \begin{bmatrix} 0 & 1 \\ 0 & 0 \end{bmatrix} \otimes \mathbf{K}_{xy} + \begin{bmatrix} 0 & 0 \\ 1 & 0 \end{bmatrix} \otimes \mathbf{K}_{yx} + \begin{bmatrix} 0 & 0 \\ 0 & 1 \end{bmatrix} \otimes \mathbf{K}_{yy} = \begin{bmatrix} \mathbf{K}_{xx} & \mathbf{K}_{xy} \\ \mathbf{K}_{yx} & \mathbf{K}_{yy} \end{bmatrix}, \quad (28)$$

and

$$\mathbf{f} = \begin{bmatrix} 1 \\ 0 \end{bmatrix} \otimes \mathbf{f}_x + \begin{bmatrix} 0 \\ 1 \end{bmatrix} \otimes \mathbf{f}_y = \begin{bmatrix} \mathbf{f}_x \\ \mathbf{f}_y \end{bmatrix}. \quad (29)$$

Using the stiffness matrix and the RHS load vector defined above, we solve the resulting linear system  $\mathbf{K}\mathbf{u} = \mathbf{f}$  for the displacement field solution  $\mathbf{u}$  on employing the AMEn solver [35].

### 3.8. Dirichlet boundary conditions

We focus on how to impose Dirichlet boundary conditions at the subdomain level. Each one of the four sides of every subdomain can be either constrained via horizontal or vertical rollers or clamped, where both horizontal and vertical displacements are constrained; see, cf. [28].

Overall, the set of all possible combinations of boundary conditions in the two-dimensional vector case is spanned by the following one-dimensional vectors:

$$\begin{aligned} \mathbf{X}_{01} &= \underbrace{[0, 1, 1, \dots, 1, 1]}_{1,2,3,\dots,2^d-1,2^d}, \underbrace{[1, 1, \dots, 1, 1]}_{1,2,3,\dots,2^d-1,2^d}, \quad \mathbf{X}_{10} = \underbrace{[1, 1, 1, \dots, 1, 0]}_{1,2,3,\dots,2^d-1,2^d}, \underbrace{[1, 1, \dots, 1, 1]}_{1,2,3,\dots,2^d-1,2^d}, \\ \mathbf{Y}_{01} &= \underbrace{[1, 1, 1, \dots, 1, 1]}_{1,2,3,\dots,2^d-1,2^d}, \underbrace{[0, 1, \dots, 1, 1]}_{1,2,3,\dots,2^d-1,2^d}, \quad \mathbf{Y}_{10} = \underbrace{[1, 1, 1, \dots, 1, 1]}_{1,2,3,\dots,2^d-1,2^d}, \underbrace{[1, 1, \dots, 1, 0]}_{1,2,3,\dots,2^d-1,2^d}, \\ \mathbf{XY}_{01} &= \underbrace{[0, 1, 1, \dots, 1, 1]}_{1,2,3,\dots,2^d-1,2^d}, \underbrace{[0, 1, \dots, 1, 1]}_{1,2,3,\dots,2^d-1,2^d}, \quad \mathbf{XY}_{10} = \underbrace{[1, 1, 1, \dots, 1, 0]}_{1,2,3,\dots,2^d-1,2^d}, \underbrace{[1, 1, \dots, 1, 0]}_{1,2,3,\dots,2^d-1,2^d}, \end{aligned}$$



where 0 stands for constrained degrees of freedom (dofs) and 1 for free dofs. When the sides are free, the corresponding boundary vector is

$$\mathbf{XY}_{11} = \underbrace{[1, 1, 1, \dots, 1, 1]}_{1,2,3,\dots,2^d-1,2^d} \underbrace{[1, 1, \dots, 1, 1]}_{1,2,3,\dots,2^d-1,2^d}. \quad (30)$$

The boundary masks are then generated through the Kronecker product of the relevant vectors. For example, when we eliminate either the nodal  $x$ - or  $y$ -displacements at the left ( $L$ ) and right ( $R$ ) side of the two-dimensional domain, the masks to be applied are the following:

$$\begin{aligned} \mathbf{M}_{XL} &= \mathbf{XY}_{11}^T \otimes \mathbf{X}_{01}, & \mathbf{M}_{XR} &= \mathbf{XY}_{11}^T \otimes \mathbf{X}_{10}, \\ \mathbf{M}_{YL} &= \mathbf{XY}_{11}^T \otimes \mathbf{Y}_{01}, & \mathbf{M}_{YR} &= \mathbf{XY}_{11}^T \otimes \mathbf{Y}_{10}. \end{aligned}$$

The z-ordered mask matrices are then obtained by replacing the Kronecker product  $\otimes$  with the z-Kronecker product  $\circ$  [28]. Then, a flattened version of the masks is constructed following the procedure indicated in [28].

### 3.8.1. Algorithm

We summarize all process algorithmic procedures in scheme 1

## 4. Low-rank TT and QTT formats for solver data representation

Hereafter, we briefly introduce the concept of tensor train [5, 7] and quantized tensor train formats [14, 16] for low-rank tensor representations and discuss how we use these formats in our algorithm's design. The key point is that by approximating the PDE solution, which is represented by a high-dimensional tensor with low-rank TT or QTT format, we can efficiently capture the essential solution features without storing the entire solution, hence leading to faster computations.

The **TT format representation** of a tensor is a compressed representation that makes it possible to store in memory and efficiently manipulate high-dimensional low-rank tensors. This task is achieved by breaking down a  $d$ -dimensional tensor into a product of two matrices and  $(d - 2)$  three-dimensional tensors, called the *cores*. Let  $\mathcal{T} \in \mathbb{R}^{n_1 \times \dots \times n_d}$  be a  $d$ -dimensional tensor, whose elements are addressed as  $\mathcal{T}(i_1, \dots, i_d)$ , with  $i_\ell = 1, \dots, n_\ell$  for  $\ell = 1, \dots, d$ . We refer to  $n_\ell$  as the *mode size* (or, simply, the *size*) of the  $\ell$ -th dimension, and to the corresponding index  $i_\ell$  as the *mode index* (or, simply, the *index*) associated with such dimension. Tensor  $\mathcal{T}$  is said to be in TT-format if there exists  $d$  three-dimensional cores, denoted as  $T_\ell \in \mathbb{R}^{r_{\ell-1} \times n_{\ell} \times r_\ell}$  for  $\ell = 1, \dots, d$ , such that

$$\mathcal{T}(i_1, i_2, \dots, i_{d-1}, i_d) = T_1(:, i_1, :) T_2(:, i_2, :) \dots T_{d-1}(:, i_{d-1}, :) T_d(:, i_d, :)$$

for all possible combinations of the indices  $i_1, i_2, \dots, i_d$ , and using a Matlab-like notation to express the matrix-matrix multiplication. The numbers  $r_\ell$  for  $\ell = 0, 1, \dots, d$  are called the *representation ranks* (or, simply, the *ranks*) of the TT-format representation. We assume that  $r_0 = r_d = 1$ , so that the first and last core, i.e.,  $T_1$  and  $T_d$  are, indeed, matrices. By expanding the compact core-matrix

---

**Algorithm 1** Global Finite Element Assembly in QTT format with nodal Z-ordering

---

**Input:**

- $\Omega$ : The computational domain
- $q$ : Number of subdomains
- $d$ : Number of QTT dimensions
- $\mathbf{f}(x, y), (x, y) \in \Omega$ : forcing term
- $\mathbf{u}_0(x, y), (x, y) \in \partial\Omega$ : boundary displacement on  $\partial\Omega$  for Dirichlet boundary conditions

**Output:**

- $\mathbf{K}$ : Global stiffness matrix
  - $\mathbf{f}$ : Global force vector
- 1: Partition  $\Omega$  into  $q$  subdomains  $\{\Omega^{(m)}\}_{m=1,2,\dots,q}$
  - 2: Generate a local quadrilateral mesh with  $2^d \times 2^d$  partition elements in each subdomain  $\Omega^{(m)}$
  - 3: Introduce the Z-ordering nodal numbering system in each subdomain
  - 4: **for**  $m = 1$  **to**  $n$  **do**
  - 5:     **for each** element  $(i, j)$  in  $\Omega^{(m)}$  **do** with  $i, j = 1, 2, \dots, 2^d$
  - 6:         Compute the Jacobian matrix  $\mathbf{J}^{i,j}(\xi, \eta)$  (see the expansion of Eq.(19) and subsection 3.4)
  - 7:         Initialize local stiffness matrix  $\mathbf{K}^{(m)}$  and force vector  $\mathbf{f}^{(m)}$  to zero.
  - 8:         **for** every reference node  $(c_1, c_2) \in \{(-1, -1), (1, -1), (1, 1), (-1, 1)\}$  **do**
  - 9:             Compute matrices  $\mathcal{K}_{(c_1, c_2)}$ , and  $\mathbf{G}_{c_1, c_2}$  and shift matrices  $\mathbf{V}_{c_1}, \mathbf{V}_{c_2}$
  - 10:             Compute  $\mathbf{K}_{(c_1, c_2)}^{(m)} \leftarrow \mathbf{V}_{c_1}^T \text{diag}(\mathcal{K}_{(c_1, c_2)}) \mathbf{V}_{c_2}$ , (see Eq. (21))
  - 11:             Compute  $\mathbf{f}_{c_1, c_2}^{(m)} \leftarrow \mathbf{V}_{c_1}^T \text{diag}(\mathbf{G}_{c_1, c_2}) \mathbf{V}_{c_2} \bar{\mathbf{f}}$  (see Eq. (23))
  - 12:             Assemble  $\mathbf{K}_{(c_1, c_2)}^{(m)}$  into  $\mathbf{K}^{(m)}$  (see Eq. (22) and subsection 3.5)
  - 13:             Assemble  $\mathbf{f}_{c_1, c_2}^{(m)}$  into  $\mathbf{f}^{(m)}$  (see Eq. (24) and subsection 3.5)
  - 14:         **end for**
  - 15:     **end for**
  - 16: **end for**
  - 17: Assemble global  $\mathbf{K}$  and  $\mathbf{f}$  from  $\{\mathbf{K}^{(m)}\}$  and  $\{\mathbf{f}^{(m)}\}$  (see subsection 3.6)
  - 18: Apply boundary conditions to  $\mathbf{K}$  and  $\mathbf{f}$  (see subsection 3.8)
  - 19: **return**  $\mathbf{K}, \mathbf{f}$
- 

representation above (and omitting the trivial summation over the indices  $\alpha_0$  and  $\alpha_d$  ranging from 1 to 1), we find the equivalent entry-wise formulation:

$$\begin{aligned} \mathcal{T}(i_1, i_2 \dots i_{d-1}, i_d) &= \sum_{\alpha_1=1}^{r_1} \sum_{\alpha_2=1}^{r_2} \dots \sum_{\alpha_{d-1}=1}^{r_{d-1}} T_1(i_1, \alpha_1) T_2(\alpha_1, i_2, \alpha_2) \dots \\ &\quad \dots T_{d-1}(\alpha_{d-2}, i_{d-1}, \alpha_{d-1}) T_d(\alpha_{d-1}, i_d). \end{aligned}$$

The tensor train decomposition is particularly useful in the case where the ranks are much smaller than the mode sizes, i.e.,  $r_\ell \ll n_\ell$  for all tensor dimensions  $\ell = 1, \dots, d$ . The amount of memory required for storing  $T$  is  $\text{storage} = r_1 n_1 + \sum_{i=2}^{d-1} r_{i-1} n_i r_i + r_{d-1} n_d$ , which grows proportionally to

$\mathcal{O}(dr^2n)$ , where  $r = \max(r_1, \dots, r_{d-1})$  and  $n = \max(n_1, \dots, n_d)$  are convenient upper bounds on the ranks and mode sizes. Following [28], we introduce the *effective rank*, which we denote by  $r_e$  and occasionally abbreviate as *erank*. This quantity is a sort of average rank for the cores of the tensor train representation of  $\mathcal{T}$  and satisfies, by definition, the condition

$$r_e n_1 + \sum_{i=2}^{d-1} r_e^2 n_i + r_e n_d = \text{storage of } T.$$

On solving the equation above, it follows immediately that  $r_e = \mathcal{O}(\sqrt{\text{storage of } T})$

In the case of second-order elliptic partial differential equations in two dimensions [30], the quantized tensor-structured solver applied to  $q$  subdomains has been characterized in terms of the maximum rank  $R_d$

$$R_d = \max_{0 \leq i < d} r_d, \quad (31)$$

and the number of parameters  $N_d$  involved in the representation defined as follows:

$$N_d = qr_0 + \sum_{i=1}^{d-1} 2^2 r_{i-1} r_i + 2^2 r_{d-1} = \mathcal{O}(dR_d^2). \quad (32)$$

Now, consider the *multi-index representation* of the tensor elements. Let  $\underline{i} = (i_1, \dots, i_d)$  a  $d$ -dimensional multi-index, where every component  $i_\ell$  is a non-negative integer number, and  $|\underline{i}| = i_1 + \dots + i_d$  is the *order* of  $\mathbf{i}$ . Then, we address the elements of tensor  $T$  as  $T(\underline{i}) := T(i_1, \dots, T_d)$ . Since  $T$  has a single multi-index, we can interpret it as a “*vector*” tensor (a vector is an object with a single index), and it is straightforward to introduce the concept of a “*matrix*” tensor, i.e., a *multi-dimensional matrix* whose elements are indexed by two multi-indices  $\underline{i}$  and  $\underline{j}$ , e.g.,  $\mathcal{A}(\underline{i}, \underline{j})$ . For consistency, these multi-indices must have the same number of dimensions  $d$ , so that we can pair them as  $(i_\ell, j_\ell)$  for  $\ell = 1, \dots, d$ , although the mode sizes can be different. Let  $i_\ell = 1, \dots, n_\ell$  (as above), and  $j_\ell = 1, \dots, m_\ell$  for  $\ell = 1, \dots, m_\ell$ . A  $d$ -dimensional matrix tensor  $\mathcal{A}$  is said to be in tensor-train format if there exist  $d$  four-dimensional tensor said *cores*  $A_\ell \in \mathbb{R}^{r_{\ell-1}, n_\ell, m_\ell, r_\ell}$  with  $r_1 = r_d = 1$  such that

$$\begin{aligned} \mathcal{A}(\underline{i}, \underline{j}) &:= \mathcal{A}((i_1, \dots, i_d), (j_1, \dots, j_d)) \\ &= A_1(:, i_1, j_1, :) A_2(:, i_2, j_2, :) \cdots A_{d-1}(:, i_{d-1}, j_{d-1}, :) A_d(:, i_d, j_d, :) \end{aligned}$$

for all possible combinations of the index pairs  $(i_1, j_1), \dots, (i_d, j_d)$ , using again a Matlab-like notation to express the matrix-matrix multiplication. The equivalent entry-wise expression is

$$\begin{aligned} \mathcal{A}((i_1, \dots, i_d), (j_1, \dots, j_d)) &= \\ &= \sum_{\alpha_1=1}^{r_1} \sum_{\alpha_2=1}^{r_2} \cdots \sum_{\alpha_{d-2}=1}^{r_{d-2}} \sum_{\alpha_{d-1}=1}^{r_{d-1}} A_1(i_1, j_1, \alpha_1) A_2(\alpha_1, i_2, j_2, \alpha_2) \cdots \\ &\quad \cdots A_{d-1}(\alpha_{d-2}, i_{d-1}, j_{d-1}, \alpha_{d-1}) A_d(\alpha_{d-1}, i_d, j_d), \end{aligned}$$

and again omitting the trivial summation over  $\alpha_0$  and  $\alpha_d$ .

**Remark 4.1.** We can treat each pair  $i_\ell, j_\ell$  as one “long index”, e.g.,  $k_\ell = i_\ell + n_\ell(j_\ell - 1)$  ranging from 1 to  $n_\ell m_\ell$ . Moreover, we can consider each core  $A_\ell$  as a block matrix of dimensions  $(r_{\ell-1} n_\ell) \times (r_\ell m_\ell)$ . This block matrix is split into an  $r_{\ell-1} \times r_\ell$  block structure. The block  $A_\ell(\alpha_{\ell-1}, :, :, \alpha_\ell)$ , which is addressed by the index pair  $(\alpha_{\ell-1}, \alpha_\ell)$ , for  $\alpha_{\ell-1} = 1, 2, \dots, r_{\ell-1}$ ,  $\alpha_\ell = 1, 2, \dots, r_\ell$ , is the  $n_\ell \times m_\ell$ -sized matrix block, whose  $(i_\ell, j_\ell)$ -th element is  $A_\ell(\alpha_{\ell-1}, i_\ell, j_\ell, \alpha_\ell)$ .

An alternative formulation makes use of the *strong Kronecker product* denoted as  $\bowtie$ . The strong Kronecker product is a block matrix operation applied to block sub-matrices, similar to the regular matrix product, but with the key difference that it multiplies entire blocks using the (regular) Kronecker product  $\otimes$  instead of multiplying individual elements. For example, consider matrices  $K = (K_{IJ})$  and  $L = (L_{I'J'})$  that are partitioned into smaller sub-matrices (or blocks)  $K_{Ij}$  and  $L_{I'j'}$  whose position inside, respectively,  $K$  and  $L$  is determined by the block index pair “ $IJ$ ” and “ $I'J'$ ”. In the strong Kronecker product between matrices  $K$  and  $L$  the element at position  $((IJ), (I'J'))$  is the Kronecker product of the corresponding subblocks, and is formally expressed as:

$$(K \bowtie L)_{((IJ), (I'J'))} = K_{IJ} \otimes L_{I'J'}.$$

Using the strong Kronecker product, we can write  $\mathcal{A}$  in TT format in terms of its cores  $\{A_\ell\}_{1 \leq \ell \leq d}$  as

$$\mathcal{A} = A_1 \bowtie A_2 \bowtie \dots \bowtie A_{d-1} \bowtie A_d.$$

**Remark 4.2.** If all the internal ranks of tensor  $\mathcal{A}$  are equal to 1, we can write it as the regular Kronecker product of the  $d$  matrices  $A_\ell(1, :, :, 1) \in \mathbb{R}^{n_\ell \times m_\ell}$ ,  $\ell = 1, 2, \dots, d$ :

$$\mathcal{A} = A_1 \otimes A_2 \otimes \dots \otimes A_{d-1} \otimes A_d,$$

with the obvious extension of the Kronecker product from two to  $d$  arguments.

Following [28], we will use the **QTT-format representation** and adopt the “*Z-order*” that we will extend to the vector case in the next section. QTT is a special tensor train format that can be applied to represent both vector and matrices. To obtain a QTT representation of such objects, we first reshape them into a multidimensional *binary* tensor representation, where “binary” that the size of every dimension is 2, and then we perform a tensor train decomposition. The motivation for using QTT is its low memory consumption, with low-rank approximations and speed in solving linear equation systems. We will employ the QTT format to compute and store all the components of the final linear system. Then, we will solve this system by using the AMEn solver, which is designed explicitly for TT representations to take advantage of the low-rank structure when present, hence leading to faster convergence and reduced computation time.

Using QTT improves efficiency in solving differential equations through several key mechanisms. QTT reduces the complexity of representing matrix operators and solution vectors from polynomial, e.g.,  $\mathcal{O}(N^2)$ , to logarithmic, e.g.,  $\mathcal{O}(\log(N))$ , where  $N$  is the total number of degrees of freedom. Such reduction to a logarithmic complexity drastically decreases both memory usage

and computational cost. For example, we can reshape a vector  $\mathbf{v} \in \mathbb{R}^{2^d}$  as a  $d$ -dimensional tensor  $\mathcal{V}$  of dimension  $2 \times 2 \times \dots \times 2$  ( $d$  times); we consider its TT format representation with ranks  $r_1, \dots, r_{d-1}$ ; we reshape vector  $\mathbf{v}$  into the  $d$ -dimensional tensor  $\mathcal{V}$  encoding the index value of  $\mathbf{v}$ , e.g.,  $1 \leq i \leq 2^d$ , into the binary format:

$$i = \overline{i_1, i_2, \dots, i_d} = \sum_{k=1}^d 2^{k-1} i_k \leftrightarrow (i_1, i_2, \dots, i_d)$$

We can use the same idea to represent a matrix in the QTT format. In such a case, we formally find that  $\mathcal{A} \in \mathbb{R}^{2^d \times 2^d}$ . According to [28], we will reorder the matrices elements in the  $Z$ -order to prevent unnecessary rank growth during computations and make use of operations like  $z$ -kron to manipulate these mathematical objects efficiently.

## 5. Numerical examples

This section is devoted to the assessment of the convergence properties of QTT-FEM compared to classic sparse FEM solvers in a series of structural plane stress examples that require accurate discretization to overcome the poor performance of low-order elements such as in beam bending problems or because of geometric singularities. In the former case, bending in the cantilever beam as in Figure 2(a) is studied having a height-to-length ratio equal to 20. For this geometry, 20 subdomains were used, each with a grid of  $2^d \times 2^d$  nodes. A red vertical line separates adjacent subdomains, and each subdomain is partitioned by a  $3 \times 3$ -square grid and denoted by  $\Omega^{(m)}$ ,  $m = 1, 2, \dots, 20$ . Then, a standard tensile single-edge notched (SEN) specimen and an L-shaped plate are modeled as examples of possible applications relevant to solid mechanics engineering, see, e.g., [38]. The corresponding geometries are displayed in Figures 2(b)-2(c), assuming  $d = 2$  levels and  $q = 2$  subdomains and  $d = 3$  levels and 3 subdomains, respectively. Both the SEN and the L-shaped plate have a length of  $\ell = 1$  mm and are subjected to a traction  $t = 3$  MPa. In all these examples, we assume the material to be isotropic with Young modulus  $E = 64$  MPa and a vanishing Poisson ratio.

### 5.1. Convergence properties

The present section is dedicated to the study of the convergence properties of the QTT finite element solver. In particular, we compare the performance of our QTT approach with that of FEniCS [39], a classical sparse matrix finite element software.

According to [37, 38, 40], we evaluate  $E = \|\mathbf{u}_{QTT} - \mathbf{u}_{ref}\|$ , the error in the energy seminorm, and  $E_{\mathbb{L}^2} = \|\mathbf{u}_{QTT} - \mathbf{u}_{ref}\|_{\mathbb{L}^2}$ , the error in the  $\mathbb{L}^2$ -norm. The notation  $\mathbf{u}_{QTT}$  identifies the displacement solution obtained with the QTT solver, while the reference solution  $\mathbf{u}_{ref}$  is the displacement evaluated with FEniCS with an overrefined mesh consisting of 7242852 degrees of freedom (dofs). Figures 3(a)-3(b) illustrate the convergence rates in the cantilever test for different levels of approximation tolerance  $\varepsilon$  of the AMEn solver. In these figures, we plot the errors in both the energy seminorm and the  $\mathbb{L}^2$ -norm. For comparison, we show the results obtained by using FEniCS and the expected slopes of convergence for the P1-approximation. The convergence slope for the L-shaped panel concurs with the literature value [38]. The trend of the QTT solver results is consistent with

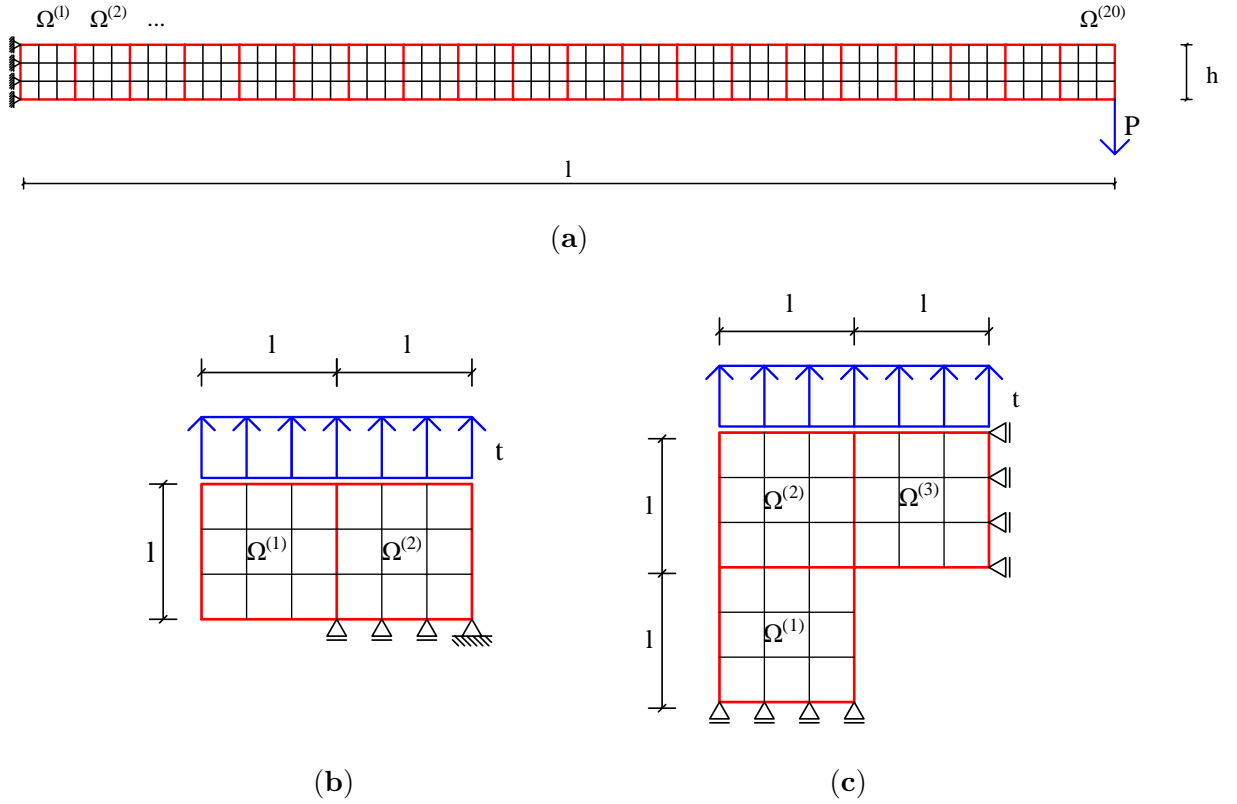


Figure 2: Geometry, boundary conditions, and representative meshes for the test cases of Section 5. (a) Cantilever beam test case assuming  $d = 2$  levels and  $q = 20$  subdomains. (b) Single edge notch tensile test case with  $d = 2$  levels and  $q = 2$  subdomains. (c) L-shaped domain test case with  $d = 3$  levels and  $q = 3$  subdomains. Red vertical and horizontal lines separate adjacent subdomains; each subdomain is partitioned by a  $3 \times 3$ -square grid, and denoted by  $\Omega^{(m)}$ .

the expected convergence rates up to a certain value of the number of degrees of freedom beyond which it drifts apart because of the rounding errors stemming from both limited machine precision and AMEn approximation prevail [24, 28].

### 5.2. Memory storage saving

Figures 5(a), 5(c), and 5(e) highlight the drastic memory cut of the QTT memory storage compared to the memory storage required by FEniCS for increasing degrees of freedom. FEniCS results exhibit indeed a vertiginous peak of memory consumption. Remarkably, this memory-peak-cut ability is quite stable when assessed for different approximation accuracies  $\varepsilon$  of the AMEn solver.

The effective rank  $r_e$  (erank) is also plotted as a function of the dofs in Figures 5(b), 5(d) and 5(f). The exhibited asymptotic trend of  $r_e$  is a consequence of adopting the Z-order-based

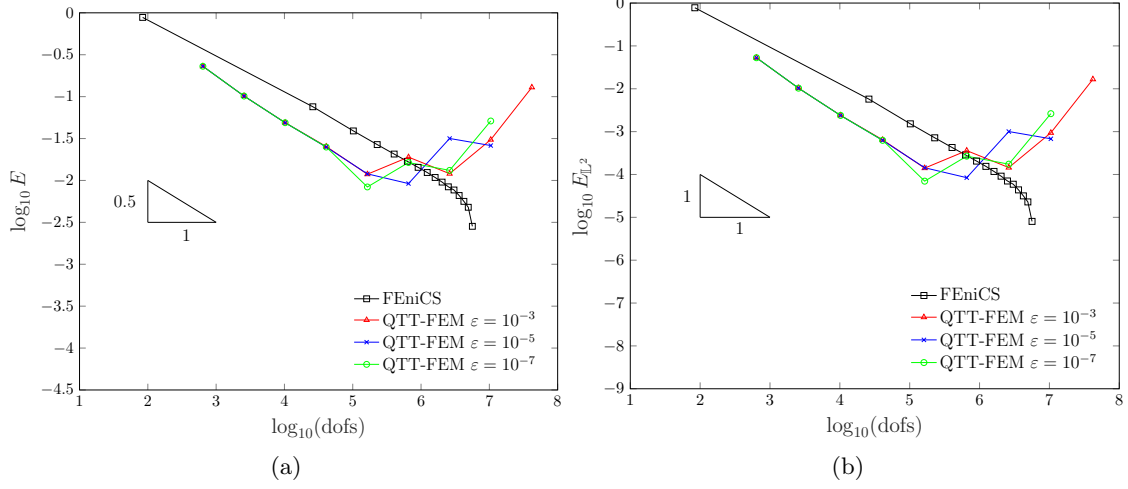


Figure 3: Cantilever beam test case: bilogarithmic plot of QTT and FEniCS energy seminorm (a) and  $L^2$ -norm (b) errors for different AMEn approximation accuracy.

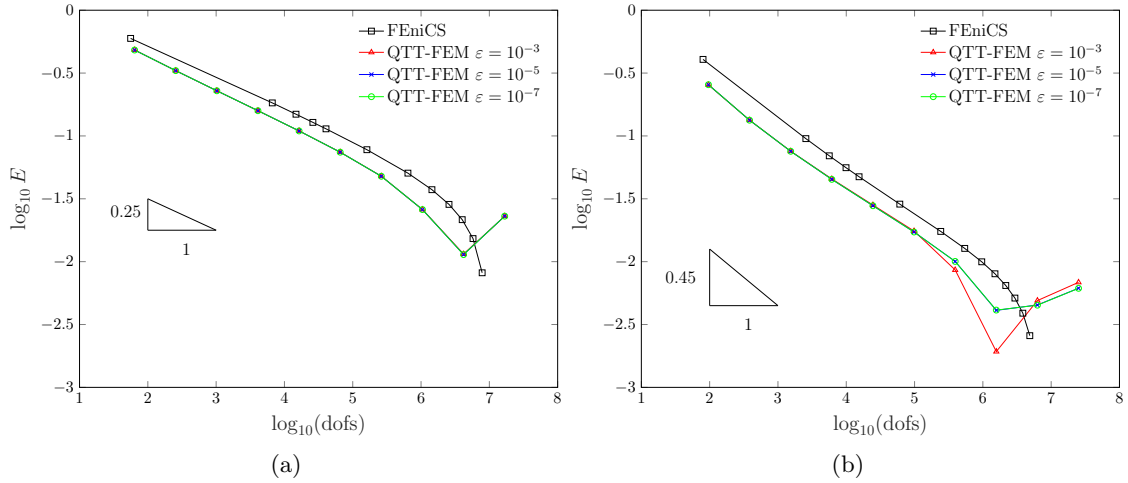


Figure 4: Energy seminorm error assuming different AMEn approximation accuracies for the single edge notch tensile test (a) and the L-shaped panel (b).

Kronecker product between matrices [33]. Using the Z-ordering system instead of the canonical order is clearly a major improvement since the latter cannot achieve such an advantageous bound of the effective rank.

### 5.3. Exponential convergence

We further assessed the QTT convergence properties for all the examples here reported by assuming a tolerance  $\varepsilon = 10^{-3}$ . Precisely, we expect an exponential convergence in the vector

variable case similar to the one proved in Ref. [29], where the nodal variables are scalar quantities associated with the finite element approximation of a Poisson problem. We report the results in Figures 6, 7, and 8 for the cantilever beam test case, the SEN test case, and the L-shaped plate test case, respectively. In all such figures, the red points identify the results exhibiting the proper energy-seminorm convergence. For completeness, the grey points indicate the results that mostly appear to be affected by rounding errors.

According to [29], we display the convergence in the energy-seminorm error  $E$  for an increasing number of levels  $d$ . In this case, the continuous lines indicate the reference exponential convergence line defined by  $E = C_\alpha 2^{-\alpha d}$ , where  $C_\alpha$  is a constant factor independent of  $d$  and may change depending on the singularity order of the exact solution, and  $\alpha$  is also determined by the low-order finite element approximation. Interestingly, our results point out that  $\alpha = \min(1, \beta)$ , where  $\beta$  is twice the singularity order of the problem solution, namely  $\beta = 2, 0.5, 0.9$  for the cantilever beam, the SEN plate, and the L-shaped panel test cases, respectively.

We plot the error  $E$  in the energy semi-norm  $E$  or a variable number of parameters  $N_d$ . We use the line defined by  $\log_2^k E = -b_\alpha N_d$  as the reference line to highlight the exponential convergence. The parameters  $b_\alpha$  and  $\kappa$  are independent of  $d$ . The maximum rank of QTT approximation  $R_d$  also displays an exponential convergence in terms of the  $d$  level number. In this case, we consider the reference algebraic growth  $R_d = c_\alpha d^\theta$ , where, again,  $\theta$  and  $c_\alpha$  are independent of  $d$ . Finally, the number of parameters  $N_d$  versus  $d$  level number is shown together with the reference algebraic growth  $N_d = C_\alpha d^\kappa$ ,  $C_\alpha$  and  $\kappa$  being independent of  $d$ .

In the case of the cantilever beam, Figure 6(a) shows that the expected slope of convergence, which is equal to 1, is reached. Figure 6(b) illustrates the exponential convergence of the QTT-FE approximation with  $\kappa = 5$ , which represents the theoretical upper limit demonstrated for QTT-structured finite element discretization in [29]. The QTT rank  $R_d$  grows sublinearly with increasing  $d$  as shown in Figure 6(c). Finally, Figure 6(d) displays the relation between the number of levels  $d$  and the number of parameters involved in the representation  $N_d$ .

The optimal convergence rates in Figure 6(a), the exponential convergence behavior within the theoretical limit in Figure 6(b), the sublinear rank growth in Figure 6(c), and the relationship between levels and parameters (Figure 6(d)), all indicate that the QTT-FE method is performing as expected and exhibits the desired efficiency gain compared to traditional designs of the finite element method like that in FEniCS. In fact, the sublinear growth of the QTT rank when the number of levels  $d$  increases of Figure 6(c) is a clear key indicator of the CPU cost and memory savings. It demonstrates that the QTT format effectively captures the low-rank structure of the solution, leading to significant reductions in storage and computational complexity compared to the usual scaling of the finite element methods with the number of degrees of freedom. The relationship between  $d$  and  $N$  in Figure 6(d) further illustrates how the number of parameters in the QTT representation scales much more favorably than the number of degrees of freedom in a plain finite element formulation and implementation. These results validate the effectiveness of the QTT approach for this problem.

We can draw analogous conclusions for the SEN plate test case, see Figures 7(a)-7(d), and the L-shape panel test case, see Figures 8(a)-8(d). In these last cases, we note that the order of the singularity of the ground truth solution dictates the energy convergence rate for increasing



$d$  levels. These results could be improved through the AMR technique or by enriching the finite element space with additional terms that may better represent the singular behavior of the solution. However, an investigation of these methodologies is beyond the goals and scope of the present work and will be the subject of future research work.

## 6. Conclusions

We have extended the design of the Quantum Tensor Train finite element solver proposed by Markeeva et al. [33] for scalar problems to vector problems such as the linear elasticity. Combined with Z-ordering and subdomain concatenation, our approach achieves significant memory savings and remarkable rank reduction compared to traditional Finite Element solvers, such as FEniCS, all while ensuring exponential convergence versus the number of degrees of freedom. The trade-off lies in a fundamental shift in the implementation paradigm for essential finite element operations, including mesh discretization, ordering of nodes and degrees of freedom, assembly of stiffness matrices and internal nodal forces, and algebraic matrix-vector computations. In conclusion, our work confirms that using the QTT format substantially reduces the memory usage and provides a notable enhancement in computational speed compared to traditional sparse-matrix finite element solvers. Additionally, the rank growth is effectively constrained through the use of Z-order operations.

## Acknowledgments

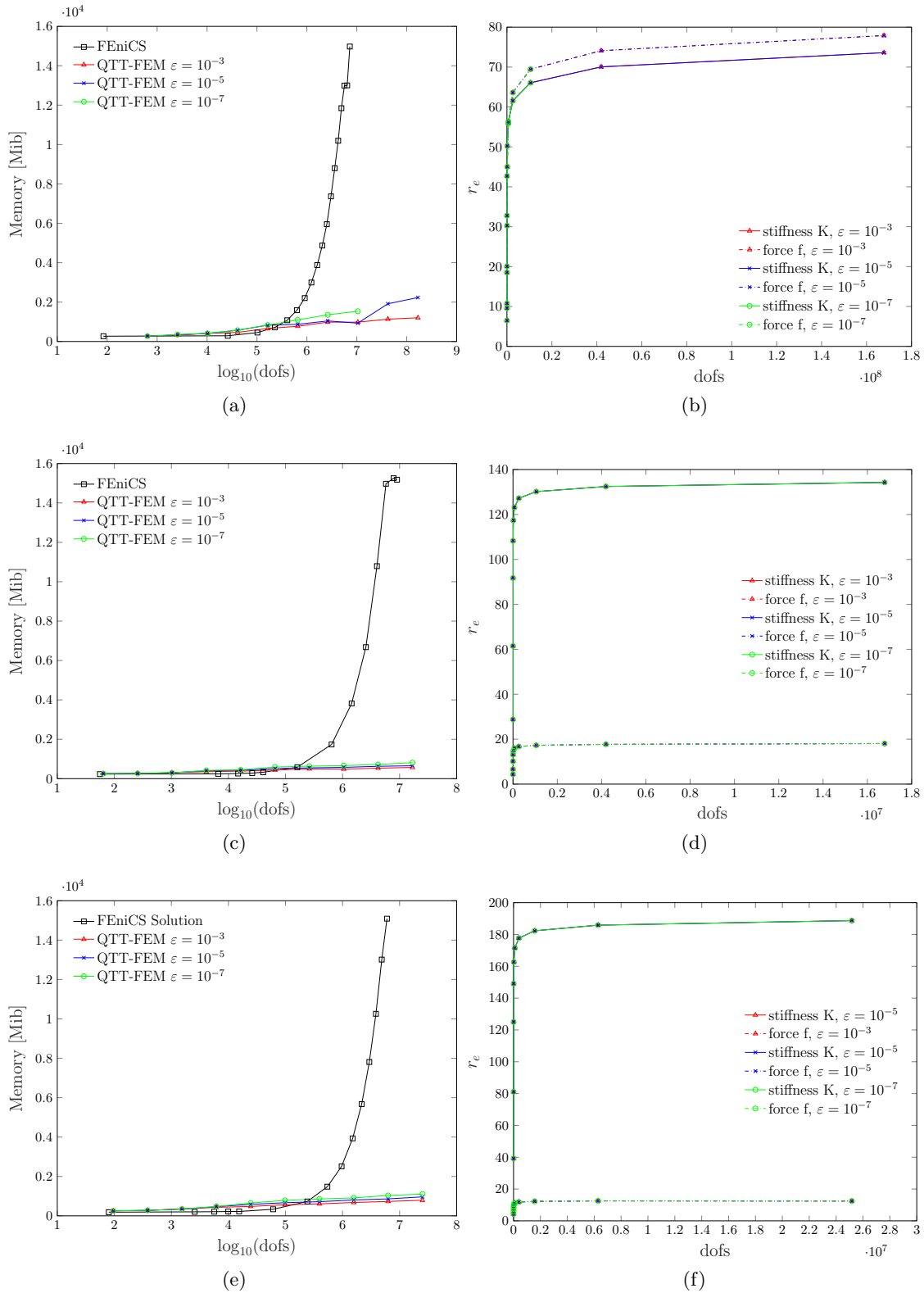
The Laboratory Directed Research and Development (LDRD) program financially supported the work of G. Manzini. Los Alamos National Laboratory is operated by Triad National Security, LLC, for the National Nuclear Security Administration of the U.S. Department of Energy (Contract No. 89233218CNA000001). G. Manzini is a member of the Gruppo Nazionale Calcolo Scientifico-Istituto Nazionale di Alta Matematica (GNCS-INdAM). E. Benvenuti, M. Nale, and S. Pizzolato gratefully acknowledge the financial support of the Italy-Croatia Interreg Project STRENGTH (ID: ITHR0200318).

## References

- [1] P. Ladevèze, J. Passieux, D. Néron, The LATIN multiscale computational method and the proper generalized decomposition, *Computer Methods in Applied Mechanics and Engineering* 199 (21-22) (2010) 1287–1296.
- [2] P. Ladevèze, *Nonlinear computational structural mechanics: New approaches and non-incremental methods of calculation*, Springer Science & Business Media, 2012.
- [3] F. Chinesta, A. Leygue, F. Bordeu, J. Aguado, E. Cueto, D. González, I. Alfaro, A. Ammar, A. Huerta, PGD-based computational vademecum for efficient design, optimization and control, *Archives of Computational Methods in Engineering* 20 (2013) 31–59.
- [4] R. Bellman, *Adaptive Control Processes: A Guided Tour*, Princeton University Press, Princeton, NJ, 1961.
- [5] I. Oseledets, Tensor-train decomposition, *SIAM, Journal on Scientific Computing* 33 (5) (2011) 2295–2317.
- [6] I. Oseledets, E. Tyrtyshnikov, TT-cross approximation for multidimensional arrays, *Linear Algebra and its Applications* 432 (1) (2010) 70–88.
- [7] I. Oseledets, E. Tyrtyshnikov, Breaking the curse of dimensionality, or how to use SVD in many dimensions, *SIAM, Journal on Scientific Computing* 31 (5) (2009) 3744–3759.
- [8] I. V. Oseledets, On a new tensor decomposition, *Doklady Akademii Nauk* 427 (2) (2009) 168–169.
- [9] I. V. Oseledets, E. E. Tyrtyshnikov, Recursive decomposition of multidimensional tensors, *Doklady Akademii Nauk* 427 (1) (2009) 14–16.
- [10] U. Schollwöck, The density-matrix renormalization group in the age of matrix product states, *Annals of Physics* 326 (1) (2011) 96–192.
- [11] F. Verstraete, J. I. Cirac, Matrix product states represent ground states faithfully, *Physical Review B* 73 (2006) 094423.
- [12] G. Vidal, Efficient classical simulation of slightly entangled quantum computations, *Physical Review Letters* 91 (2003) 147902.
- [13] S. R. White, Density-matrix algorithms for quantum renormalization groups, *Physical Review B* 48 (1993) 10345–10356.
- [14] B. Khoromskij,  $o(d \log n)$ -Quantics approximation of  $n$ -d tensors in high-dimensional numerical modeling, *Constr. Approx.* 34 (2) (2011) 257–280.
- [15] I. Oseledets, Approximation of matrices with logarithmic number of parameters, *Doklady Mathematics* 80 (2) (2009) 653–654.

- [16] I. Oseledets, Approximation of  $2^d \times 2^d$  matrices using tensor decomposition, SIAM, Journal on Matrix Analysis and Applications 31 (4) (2010) 2130–2145.
- [17] L. Grasedyck, Polynomial approximation in hierarchical tucker format by vector-tensorization, Tech. rep., Institut für Geometrie und Praktische Mathematik (2010).
- [18] V. Kazeev, B. Khoromskij, Low-rank explicit QTT representation of the Laplace operator and its inverse, SIAM J. Matrix Anal. Appl. 33 (3) (2012) 742–758.
- [19] V. A. Kazeev, B. N. Khoromskij, E. E. Tyrtshnikov, Multilevel Toeplitz matrices generated by tensor-structured vectors and convolution with logarithmic complexity, SIAM J. Sci. Comput. 35 (3) (2013) A1511–A1536.
- [20] B. N. Khoromskij, Tensor numerical methods in scientific computing, Vol. 19 of Radon Series on Computational and Applied Mathematics, De Gruyter, Berlin, 2018.
- [21] S. V. Dolgov, B. N. Khoromskij, I. V. Oseledets, Fast solution of parabolic problems in the tensor train/quantized tensor train format with initial application to the Fokker-Planck equation, SIAM J. Sci. Comput. 34 (6) (2012) A3016–A3038.
- [22] V. Kazeev, M. Khammash, M. Nip, C. Schwab, Direct solution of the chemical master equation using quantized tensor trains, PLOS Computational Biology 10 (3) (2014) 742–758.
- [23] V. Kazeev, C. Schwab, Quantized tensor-structured finite elements for second-order elliptic PDEs in two dimensions, Numer. Math. 138 (1) (2018) 133–190.
- [24] M. Bachmayr, V. Kazeev, Stability of low-rank tensor representations and structured multilevel preconditioning for elliptic PDEs, Foundations of Computational Mathematics 20 (5) (2020) 1175–1236.
- [25] V. Kazeev, I. Oseledets, M. Rakhuba, C. Schwab, QTT-finite-element approximation for multiscale problems I: model problems in one dimension, Advances in Computational Mathematics 43 (2) (2017) 411–442.
- [26] V. Kazeev, I. Oseledets, M. Rakhuba, C. Schwab, Quantized tensor FEM for multiscale problems: Diffusion problems in two and three dimensions, Multiscale Modeling & Simulation 20 (3) (2022) 893–935.
- [27] V. Kazeev, O. Reichmann, C. Schwab, Low-rank tensor structure of linear diffusion operators in the TT and QTT formats, Linear Algebra and Its Applications 438 (11) (2013) 4204–4221.
- [28] L. Markeeva, I. Tsybulin, I. Oseledets, QTT-isogeometric solver in two dimensions, Journal of Computational Physics 424 (2021) 109835.
- [29] V. Kazeev, C. Schwab, Quantized tensor-structured finite elements for second-order elliptic PDEs in two dimensions, Numerische Mathematik 138 (2018) 133–190.

- [30] V. Kazeev, Quantized tensor-structured finite elements for second-order elliptic PDEs in two dimensions, Phd thesis, ETH Zurich, Zurich, Switzerland, <https://doi.org/10.3929/ethz-a-010554062> (2015).
- [31] S. Frascini, V. Kazeev, I. Perugia, Symplectic QTT-FEM solution of the one-dimensional acoustic wave equation in the time domain, arXiv preprint arXiv:2411.11321, submitted on 18 Nov 2024 (November 2024).
- [32] V. Kazeev, C. Schwab, Tensor approximation of stationary distributions of chemical reaction networks, *SIAM J. Matrix Anal. Appl.* 36 (3) (2015) 1221–1247.
- [33] L. Markeeva, I. Tsybulin, Building Z-permuted matrices in the QTT format, *Computational Mathematics and Mathematical Physics* 60 (12) (2020) 2108–2115.
- [34] G. Morton, *A Computer Oriented Geodetic Data Base and a New Technique in File Sequencing*, International Business Machines Company New York, 1966.
- [35] S. Dolgov, D. Savostyanov, Alternating minimal energy methods for linear systems in higher dimensions, *SIAM Journal on Scientific Computing* 36 (5) (2014) A2248–A2271.
- [36] V. Dolean, P. Jolivet, F. Nataf, *An Introduction to Domain Decomposition Methods: Algorithms, Theory, and Parallel Implementation*, Society for Industrial and Applied Mathematics, Philadelphia, PA, 2015. doi:10.1137/1.9781611974065.
- [37] K. Bathe, *Finite Element Procedures*, Prentice Hall, 2006.
- [38] O. Zienkiewicz, R. Taylor, J. Zhu, *The Finite Element Method: Its Basis and Fundamentals*, Elsevier, 2005.
- [39] I. Baratta, J. Dean, J. Dokken, M. Habera, J. Hale, C. Richardson, M. Rognes, M. Scroggs, N. Sime, G. Wells, DOLFINx: The next generation FEniCS problem solving environment, preprint (2023). doi:10.5281/zenodo.10447666.
- [40] B. Szabó, I. Babuška, *Finite element analysis: Method, verification and validation*, John Wiley & Sons, 2021.



29  
Figure 5: Cantilever beam test case: (a) memory storage versus the number of degrees of freedom for different approximation accuracy  $\varepsilon$  and (b) effective rank  $r_e$  versus the number of degrees of freedom. Single edge notch tensile test: (c) memory storage versus degrees of freedom for different values of  $\varepsilon$ , and (d) effective rank  $r_e$  versus the number of degrees of freedom. L-shaped panel: (e) memory storage versus the number of degrees of freedom for different approximation accuracy  $\varepsilon$ , and (f) effective rank  $r_e$  versus the number of degrees of freedom.

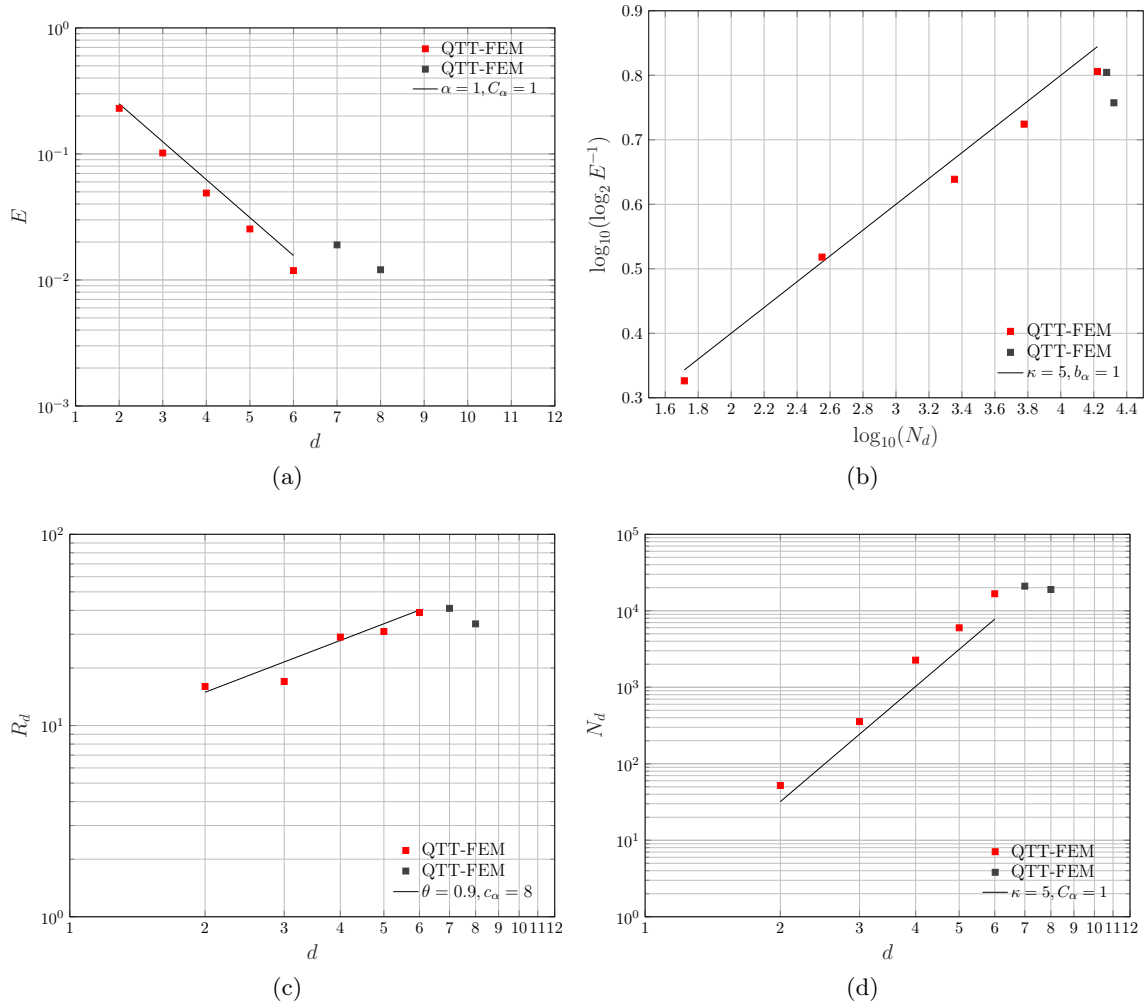


Figure 6: Cantilever beam test case: (a) Energy seminorm error  $E$  (red dots) and reference exponential convergence of equation  $C_\alpha 2^{-\alpha d}$  (continuous line) for increasing number of levels  $d$ . (b) Energy seminorm error  $E$  (red dots) and reference line  $\log_2^k E_d = -b_\alpha N_d$  for variable number of parameters  $N_d$ . (c) Maximum rank of QTT approximation  $R_d$  (red dots) and reference line  $R_d = c_\alpha d^\theta$  (continuous line) versus  $d$  levels. (d) Number of parameters  $N_d$  (red dots) and reference line  $N_d = C_\alpha d^\kappa$  (continuous line) for increasing  $d$  levels. We report the points of the numerical tests with significant rounding error in gray, while the red points indicate the expected convergence rate.

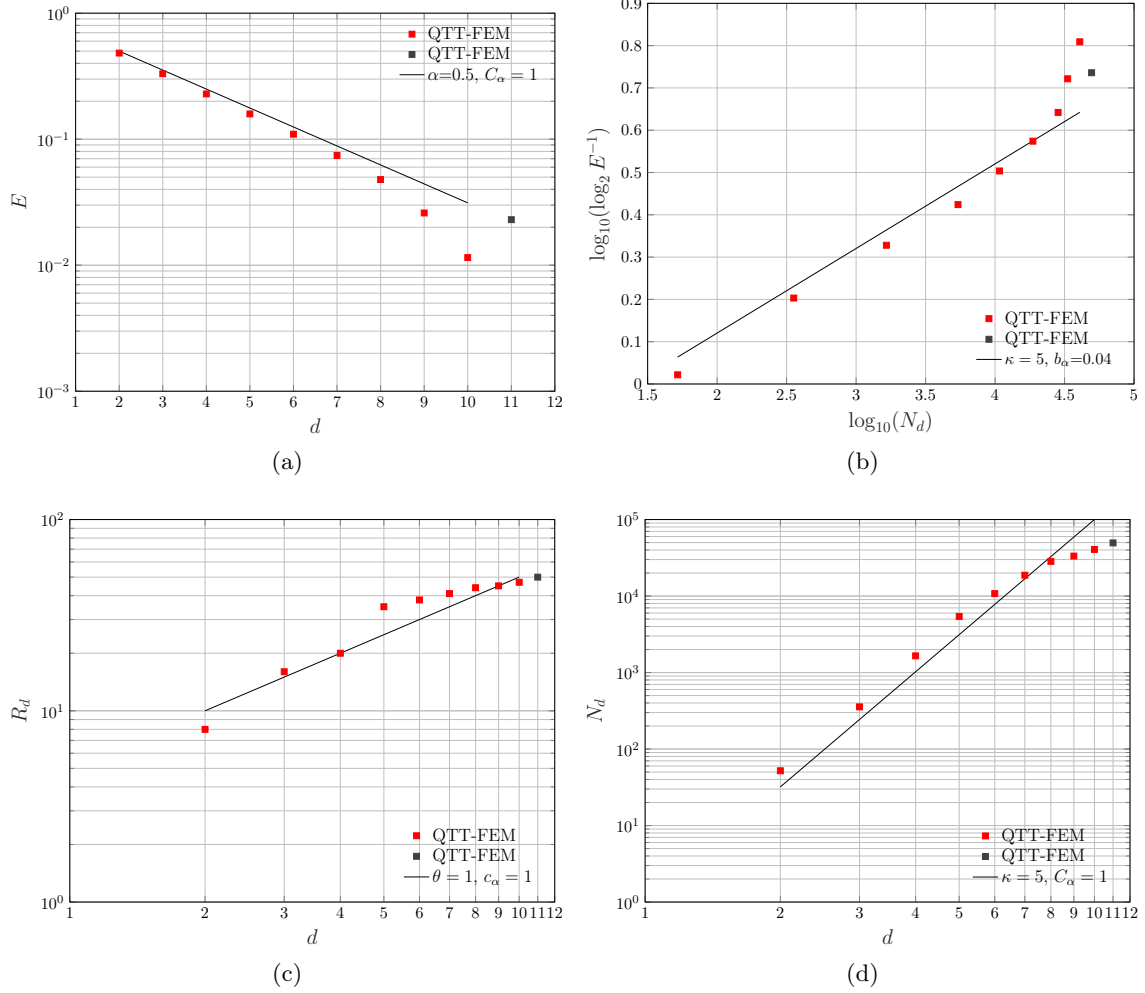


Figure 7: Single edge-notch tensile test case: (a) Energy seminorm error  $E$  (red dots) and reference exponential convergence of equation  $C_\alpha 2^{-\alpha d}$  (continuous line) for increasing number of levels  $d$ . (b) Energy seminorm error  $E$  (red dots) and reference line  $\log_2^k E_d = -b_\alpha N_d$  for variable number of parameters  $N_d$ . (c) Maximum rank of QTT approximation  $R_d$  (red dots) and reference line  $R_d = c_\alpha d^\theta$  (continuous line) versus  $d$  levels. (d) Number of parameters  $N_d$  (red dots) and reference line  $N_d = C_\alpha d^\kappa$  (continuous line) for increasing  $d$  levels. We report the points of the numerical tests with significant rounding error in gray, while the red points indicate the expected convergence rate.

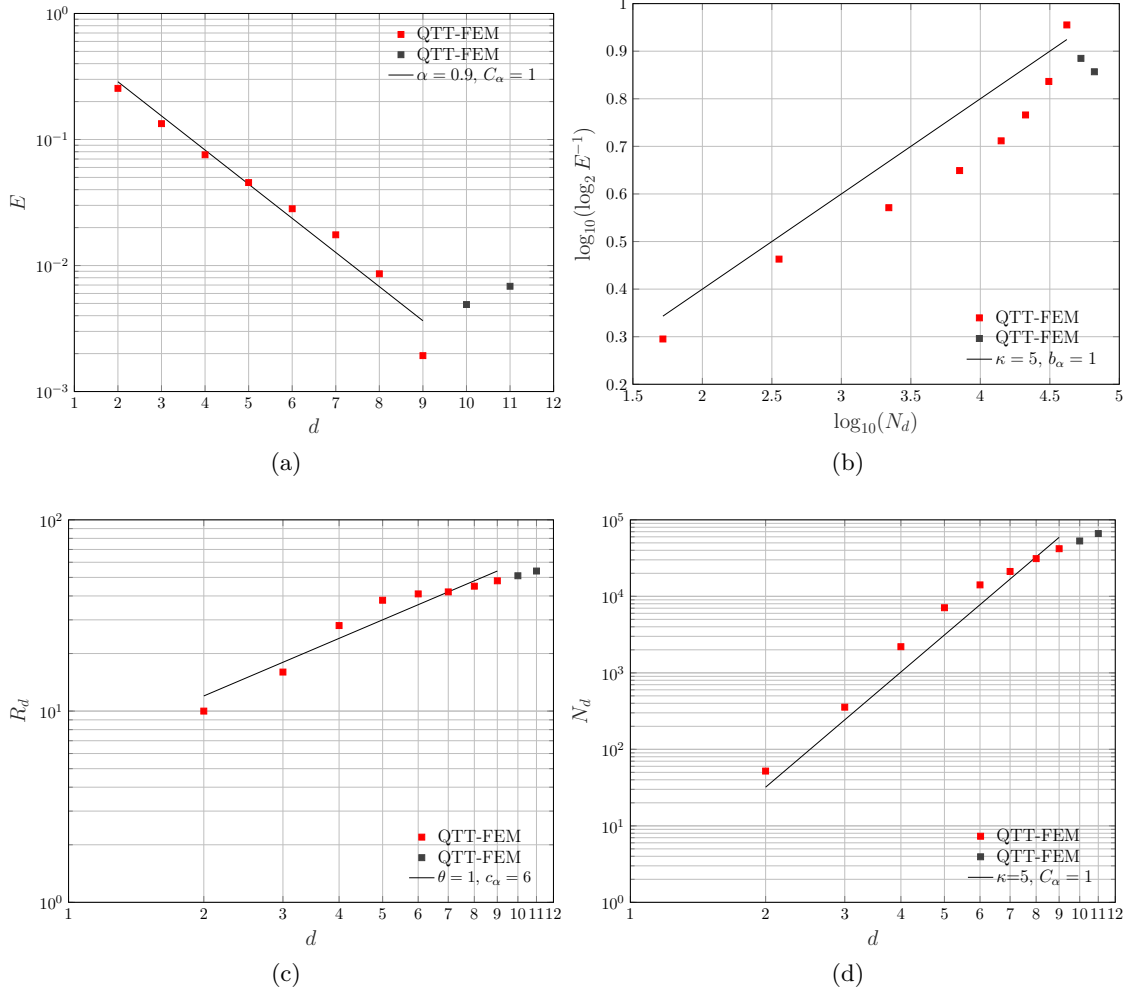


Figure 8: L-shaped panel test case: (a) Energy seminorm error  $E$  (red dots) and reference exponential convergence of equation  $C_\alpha 2^{-\alpha d}$  (continuous line) for increasing number of levels  $d$ . (b) Energy seminorm error  $E$  (red dots) and reference line  $\log_2^k E_d = -b_\alpha N_d$  for variable number of parameters  $N_d$ . (c) Maximum rank of QTT approximation  $R_d$  (red dots) and reference line  $R_d = c_\alpha d^\theta$  (continuous line) versus  $d$  levels. (d) Number of parameters  $N_d$  (red dots) and reference line  $N_d = C_\alpha d^\kappa$  (continuous line) for increasing  $d$  levels. We report the points of the numerical tests with a significant rounding error in gray, while the red points indicate the expected convergence rate.